A generalized stochastic formulation of the Ekman-Stokes model with statistical analyses

Long Li, Etienne Mémin, Bertrand Chapron

▶ **To cite this version:**

Long Li, Etienne Mémin, Bertrand Chapron. A generalized stochastic formulation of the Ekman-Stokes model with statistical analyses. 2024. hal-04672188

HAL Id: hal-04672188
https://hal.science/hal-04672188

Preprint submitted on 17 Aug 2024

HAL is a multi-disciplinary open access archive for the deposit and dissemination of scientific research documents, whether they are published or not. The documents may come from teaching and research institutions in France or abroad, or from public or private research centers.

L'archive ouverte pluridisciplinaire **HAL**, est destinée au dépôt et à la diffusion de documents scientifiques de niveau recherche, publiés ou non, émanant des établissements d'enseignement et de recherche français ou étrangers, des laboratoires publics ou privés.

Generated using the official AMS LaTeX template v6.1

A generalized stochastic formulation of the Ekman-Stokes model with statistical analyses

Long Li,[a,b] Etienne Mémin,[a,b] Bertrand Chapron,[a,c]

[a] *Odyssey Team, Centre Inria Rennes, France*

[b] *IRMAR, Université de Rennes, France*

[c] *Ifremer, Univ. Brest, CNRS, IRD, Laboratoire d'Océanographie Physique et Spatiale (LOPS), IUEM, Plouzané, France*

Corresponding author: Long Li, long.li@inria.fr

ABSTRACT: In this study, a novel stochastic formulation for the upper ocean Ekman boundary layer is derived from scaling the generalized stochastic Craik-Leibovich equations. This formulation encodes the interactions between wind, waves, and currents through the introduction of the uncertainty of unresolved motions, using established physical parameterizations. Numerical investigations of the time-dependent stochastic Ekman-Stokes model, incorporating wave mixing and stochastic transport effects, reveal Ekman velocities with an increased uncertainty, a higher kinetic energy and a stronger occurrence of extreme events, compared to traditional solutions. Stronger correlations between zonal and meridional components are obtained, with more skewed distributions and extreme values, particularly near the surface. A sensitivity analysis highlights the impact of transient winds and surface waves on statistical moments. Transient winds reduce vertical shear, deepen circulation, and increase uncertainty. Smaller surface waves also lead to higher ensemble energy and stronger correlations. Energy and transport magnitude peak when mean waves and wind are aligned, decreasing with rotation and redistributing current velocity statistics. These findings underscore the model's enhanced ability to help capture complex ocean dynamics with improved uncertainty representation.

SIGNIFICANCE STATEMENT: To describe the upper ocean Ekman boundary layer, a novel stochastic model is derived to capture the interplay between random motions induced by wind, waves, and currents. Accounting for the uncertainty of unresolved fluctuations, resulting Ekman velocities display increased variability, higher kinetic energy, and more frequent extreme events than traditional models. Near the surface, stronger correlations and skewed distributions are also revealed. Sensitivity analyses highlight impacts of transient winds and surface waves, which deepen circulation and increase uncertainty. Aligning wind and waves naturally maximizes energy and transport. This model can offer new means to describe upper ocean dynamics, providing better insights to anticipate ocean vertical fluxes and enhancing predictive capabilities.

1. Introduction

In the seminal work of Ekman (1905), an exact solution of simplified Navier–Stokes equations was obtained, fundamental to the theory of ocean circulation and attractive for theoretical analysis. The upper ocean boundary layer flow was initially conceived as steady, linear, of uniform density and viscosity, and driven solely by a surface wind stress. Owing to a balance between Coriolis and turbulent drag forces, the explicit solution displays the gradual rotation and decay of ageostrophic velocity with depth, presenting a spiral vertical structure (Vallis 2017). Several limitations in this early model have been identified, e.g. the assumption of vertically uniform eddy viscosity in the ocean (Large et al. 1994) and the significant modifications to near-surface currents induced by surface gravity waves (Huang 1979; Jenkins 1986; Xu and Bowen 1994; McWilliams et al. 1997, 2012). Buoyancy effects can also play a crucial role in the boundary layer dynamics, particularly at fronts (Price and Sundermeyer 1999; McWilliams et al. 2009; Gula et al. 2014; McWilliams et al. 2015). Although incorporating these additional effects complicates analytical solutions, advanced mathematical tools (Lewis and Belcher 2004; Wenegrat and McPhaden 2016b,a; Higgins et al. 2020) and accurate numerical methods offer viable approximations.

In this study, a stochastic approach is further considered. Building upon earlier works (Bauer et al. 2020; Mémin 2014; Resseguier et al. 2017), a stochastic approach can help statistically describe the ocean surface Ekman boundary layer. The location uncertainty framework can indeed consistently integrate the compounding effects of random winds, modulated and modulating surface waves, and turbulent mixing processes. Hereafter, we omit stratification effects, a facet to address

in future research once other interactions are clarified. By appropriately scaling the generalized stochastic Craik-Leibovich equation already outlined in Bauer et al. (2020), both steady and time-dependent stochastic Ekman-Stokes models are derived. The stochastic framework fully encodes diffusive and advective mixing effects of random fluctuations, e.g. surface winds and waves, in the vertical direction, alongside classic terms involved in the Ekman-Stokes model (Wenegrat and McPhaden 2016b,a; Higgins et al. 2020). Notably, the uncertainty representation can be consistently constrained with established physical parameterizations (McWilliams et al. 1997; McWilliams and Huckle 2006). Through large ensemble simulations, uncertainties in the Ekman boundary layer are then quantified, stemming from various random contributions (wind, waves, and turbulence), also accounting for their intermittency. Noisy fluctuations are specified to follow simple models. Specifically, the quadratic variation of these noise terms, corresponding to the process defined by the limit in probability of the square of the noise increments, matches the ideal Stokes drift of monochromatic linear waves and the K-profile-parameterization (KPP) for vertical mixing (Large et al. 1994). Yet, the resulting impacts of the noise processes are ultimately much more complex, and the system's response is not at all trivial. In this study, statistical responses are compared to those of a traditional benchmark model, followed by sensitivity analysis of the proposed random model to various wind and wave parameters.

The paper is structured as follows: Section 2 presents the proposed stochastic Ekman-Stokes models with detailed derivations and describes the uncertainty parameterization methods. Section 3 discusses the numerical results, including statistical diagnosis and sensitivity analysis of the random models. Finally, in Section 4, we draw conclusions and provide an outlook for future research endeavors.

2. Stochastic formulation

A brief review of the generalized stochastic Craik-Leibovich equations first reassesses our previous work. The stochastic Ekman-Stokes models is then derived by appropriately scaling the nonlinear equations. Subsequently, we describe the uncertainty representation induced by established physical parameterizations.

a. Review of generalized stochastic Craik-Leibovich momentum equations

The *Location Uncertainty* framework (Mémin 2014) emerges from a decomposition of the Lagrangian fluid flow into a resolved time-smooth flow component and an unresolved highly oscillating noise term:

$$\mathbf{X}_t = \mathbf{X}_0 + \int_0^t \mathbf{v}(\mathbf{X}_s, s)\,\mathrm{d}s + \int_0^t \boldsymbol{\sigma}(\mathbf{X}_s, s)\,\mathrm{d}B_s, \tag{2.1}$$

where $\mathbf{X}$ represents the stochastic Lagrangian particle trajectory, $\mathbf{v} = (u, v, w)^T$ denotes the resolved three-dimensional (3D) velocity, B is a cylindrical Brownian motion (see Da Prato and Zabczyk 2014, chap. 2) defined on an infinite-dimensional Hilbert space (function space), $\boldsymbol{\sigma} = (\sigma_x, \sigma_y, \sigma_z)^T$ is a random correlation process defined on a space of Hilbert-Schmidt operators (mapping two function spaces). More detailed mathematical descriptions on this noise term definition can be found in Debussche et al. (2023); Li et al. (2023a,b).

Several systems of stochastic partial differential equations (SPDEs), describing the evolution of key oceanic variables (such as momentum, temperature, salinity, buoyancy, and sea-surface height) transported along the stochastic flow described by Eq. (2.1) under various regimes, have been derived by Brecht et al. (2021); Li et al. (2023a); Mémin (2014); Resseguier et al. (2017); Tucciarone et al. (2024). These SPDEs are established through the application of stochastic calculus rules and adherence to fundamental physical conservation laws accompanied with classical geophysical approximations. For the Navier-Stokes equations, such stochastic approximations converge (in 2D and 3D) toward the deterministic equations as the noise vanishes (Debussche et al. 2023), providing strong consistency to this large scale representation in a similar way as grid convergence for large eddy simulations. Hereafter, we exclusively concentrate on the stochastic momentum equations governing incompressible fluid motions under the Boussinesq approximation, namely:

$$\mathrm{d}\mathbf{v} + \big((\mathbf{v} - \mathbf{v}_s)\cdot\nabla\mathbf{v} - \nabla\cdot(\boldsymbol{a}\nabla\mathbf{v}) + f\hat{\mathbf{z}}\times\mathbf{v}\big)\,\mathrm{d}t + \big(\boldsymbol{\sigma}\cdot\nabla\mathbf{v} + f\hat{\mathbf{z}}\times\boldsymbol{\sigma}\big)\,\mathrm{d}B_t = \big(b\hat{\mathbf{z}} - \nabla p\big)\,\mathrm{d}t - \nabla\mathrm{d}P_t, \tag{2.2a}$$

$$\boldsymbol{a} := \frac{1}{2}\boldsymbol{\sigma}\boldsymbol{\sigma}^T, \qquad \mathbf{v}_s := \nabla\cdot\boldsymbol{a}, \tag{2.2b}$$

$$\nabla\cdot(\mathbf{v} - \mathbf{v}_s) = 0, \qquad \nabla\cdot\boldsymbol{\sigma} = 0. \tag{2.2c}$$

Here, $\mathrm{d}v_i$ denotes the temporal variation of v_i at a fixed point, f is the Coriolis frequency, $\hat{\mathbf{z}} = (0,0,1)^T$ denotes the vertical unit vector, $b = -g\rho'/\rho_o$ is the buoyancy variable under Boussinesq approximation (where g is the gravity constant, ρ_o is the background water density, and ρ' is the density anomaly), and p represent the resolved dynamic pressure (rescaled by ρ_o).

The SPDEs (2.2a) encodes physically meaningful terms. Specifically, the term $\boldsymbol{\sigma} \cdot \nabla v_i \, \mathrm{d}B_t$ represents the random advective processes induced by unresolved fluid motions. The diffusion term, $\nabla \cdot (\boldsymbol{a} \nabla v_i)$, depicts the unresolved diffusive mixing effects associated with the random symmetric non-negative diffusion tensor $\boldsymbol{a} = \boldsymbol{\sigma}\boldsymbol{\sigma}^T/2$, also referred to the variance tensor as it corresponds to the one-point-two-times covariance matrix tensor. The nonlinear term $(\mathbf{v} - \mathbf{v}_s) \cdot \nabla v_i$ involves an effective advection velocity, which adjusts the resolved velocity $\mathbf{v}$ by removing the influence of a statistical drift $\mathbf{v}_s = \nabla \cdot \boldsymbol{a}$ that captures the inhomogeneity of the unresolved random field. This turbophoresis term, referred to *Itô-Stokes drift*, has been interpreted as a generalization of the Stokes drift in Bauer et al. (2020). Both the diffusion and corrective advection terms are rigorously derived by applying the generalized Itô formula (see Bauer et al. 2020, Appendix B).

The Coriolis terms $f\hat{\mathbf{z}} \times (\mathbf{v}\,\mathrm{d}t + \boldsymbol{\sigma}\,\mathrm{d}B_t)$ appear from a change of coordinates (from inertial to rotating) for the stochastic flow (2.1). The pressure noise $\mathrm{d}P_t/\mathrm{d}t$ (in a distribution sense) is an additional Lagrange multiplier enforcing the incompressibility of unresolved fluid motions. Note that the continuity equations (2.2c) are derived from mass conservation in the stochastic framework (Mémin 2014). These non-divergent constraints also ensures energy conservation for the derived random systems (Brecht et al. 2021; Li et al. 2023a).

To interpret the Craik-Leibovich momentum equations in the stochastic framework, Equation (2.2a) can be rewritten in an equivalent form outlining the contribution of the effective advection velocity, denoted by $\mathbf{v}^\star := \mathbf{v} - \mathbf{v}_s$ hereafter. Applying a change of variable from $\mathbf{v}$ to $\mathbf{v}^\star$ and assuming a quasi-stationary Itô-Stokes drift ($\mathrm{d}\mathbf{v}_s \approx 0$), we have

$$\begin{aligned} \mathrm{d}\mathbf{v}^\star + \left(\mathbf{v}^\star \cdot \nabla + f\hat{\mathbf{z}}\times\right)(\mathbf{v}^\star + \mathbf{v}_s)\,\mathrm{d}t + \left(\boldsymbol{\sigma} \cdot \nabla(\mathbf{v}^\star + \mathbf{v}_s) + f\hat{\mathbf{z}}\times\boldsymbol{\sigma}\right)\mathrm{d}B_t \\ = \left(b\hat{\mathbf{z}} - \nabla p + \nabla \cdot \left(\boldsymbol{a}\nabla(\mathbf{v}^\star + \mathbf{v}_s)\right)\right)\mathrm{d}t - \nabla \mathrm{d}P_t. \end{aligned} \tag{2.3}$$

Manipulating further the advection term $\mathbf{v}^\star \cdot \nabla \mathbf{v}_s$ by a classical vector calculus identity, it comes the so-called *generalized stochastic Craik-Leibovich momentum equations*:

$$\begin{aligned} &\mathrm{d}\mathbf{v}^\star + \big((\mathbf{v}^\star - \mathbf{v}_s)\cdot\nabla\mathbf{v}^\star - \nabla\cdot(\boldsymbol{a}\nabla\mathbf{v}^\star) + f\hat{\mathbf{z}}\times\mathbf{v}^\star - b\hat{\mathbf{z}} + \nabla p\big)\,\mathrm{d}t + \big(\boldsymbol{\sigma}\cdot\nabla\mathbf{v}^\star + f\hat{\mathbf{z}}\times\boldsymbol{\sigma}\big)\,\mathrm{d}B_t + \nabla\mathrm{d}P_t \\ &\quad = \big(\underbrace{-f\hat{\mathbf{z}}\times\mathbf{v}_s}_{\substack{\text{Coriolis}\\\text{Stokes}}} \underbrace{-\nabla(\mathbf{v}^\star\cdot\mathbf{v}_s)}_{\substack{\text{pressure}\\\text{correction}}} + \underbrace{\mathbf{v}_s\times(\nabla\times\mathbf{v}^\star)}_{\substack{\text{Craik-Leibovich}\\\text{vortex force}}} - \underbrace{(\nabla\times\mathbf{v}_s)\times\mathbf{v}^\star}_{\substack{\text{Itô-Stokes}\\\text{force}}} + \underbrace{\nabla\cdot(\boldsymbol{a}\nabla\mathbf{v}_s)}_{\substack{\text{Itô-Stokes}\\\text{diffusive mixing}}} \big)\,\mathrm{d}t - \underbrace{\boldsymbol{\sigma}\cdot\nabla\mathbf{v}_s\,\mathrm{d}B_t}_{\substack{\text{Itô-Stokes}\\\text{advective mixing}}}. \end{aligned} \tag{2.4}$$

The first line mirrors the structure of the stochastic Boussinesq momentum equation (2.2a), with the only difference being the substitution of $\mathbf{v}^\star$ for $\mathbf{v}$. In contrast, the second line accentuates the supplementary contributions stemming from the Itô-Stokes drift acting on $\mathbf{v}^\star$. The initial three terms share identical expressions with the Coriolis-Stokes force, Stokes-corrected pressure, and Craik-Leibovich vortex force present in the classical Craik-Leibovich momentum equation (Craik and Leibovich 1976; Leibovich 1980; McWilliams et al. 1997). However, in this formulation, the vortex force characterizes the statistical influence of the inhomogeneity carried by the diffusion tensor of the random field on the large-scale current. Therefore, this momentum equation can be viewed as a generalized stochastic representation of the Craik-Leibovich system, where the turbophoresis term supplants the Stokes drift associated with wave motion. This distinction prompts us to designate the term more broadly as the Itô-Stokes drift. It is indeed not anymore exclusively associated with waves motion but more generally with inhomogeneous unresolved small-scale fluctuations. Additionally, this stochastic formulation introduces another force, referred to herein as the *Itô-Stokes force*, which pertains to the interaction between the effective velocity and the vorticity of the Itô-Stokes drift. This force can be collectively considered with the Coriolis force to yield a corrective term. Moreover, coupling effects exist between the Itô-Stokes drift and the unresolved turbulent motions through both advective and diffusive processes, encoded by the final two terms. These terms capture surface wave mixing effects when the Itô-Stokes drift approximates a real Stokes drift.

b. Nondimensional stochastic momentum equations and scaling

The procedure is now outlined for deriving the stochastic Ekman-Stokes models by scaling the generalized stochastic Craik-Leibovich momentum equations (2.3). Specifically in this study, we

do not account for stratification effects within the boundary layer. Hence, buoyancy is assumed to remain constant (see Vallis 2017, chap. 5). Without loss of generality, we set $b = 0$ in the following.

The horizontal variables and Coriolis frequency are first scaled as $\mathbf{x} = (x, y)^T = L\widehat{\mathbf{x}}$, $\mathbf{u}^\star = (u^\star, v^\star)^T = U\widehat{\mathbf{u}}$, and $f = f_0\widehat{f}$. Here, the capital letters represent variable scales and hatted variables denote nondimensional variables. Following Pedlosky (1990, chap. 4), we adopt a change of vertical coordinates to account for stretching in the boundary layer so that $z = H\widehat{z}$, $\widehat{\zeta} = \widehat{z}/\widehat{\delta_e}$, and $\delta_e = H\widehat{\delta_e}$. Here, $\widehat{z} \neq \mathrm{O}(1)$, $\widehat{\zeta} = \mathrm{O}(1)$ and δ_e denotes the Ekman boundary layer thickness. The scales of vertical velocity $w^\star = (UH\widehat{\delta_e}/L)\,\widehat{w}$ and dynamic pressure $p = f_0 UL\,\widehat{p}$ are suggested respectively by the continuity equation (2.2c) and classical geostrophic balance.

The correlation operator is decomposed into horizontal and vertical components, $\boldsymbol{\sigma} = (\boldsymbol{\sigma}_\mathbf{x}, \sigma_z)^T$ with $\boldsymbol{\sigma}_\mathbf{x} = (\sigma_x, \sigma_y)^T$. The derived diffusion tensor can thus be decomposed into $\boldsymbol{a}_{\mathbf{xx}} = \frac{1}{2}\boldsymbol{\sigma}_\mathbf{x}\boldsymbol{\sigma}_\mathbf{x}^T$, $a_{zz} = \frac{1}{2}\sigma_z^2$, and $\boldsymbol{a}_{\mathbf{x}z} = \frac{1}{2}\boldsymbol{\sigma}_\mathbf{x}\sigma_z$. We propose scaling $\boldsymbol{a}_{\mathbf{xx}}$ and a_{zz} as horizontal and vertical eddy viscosity coefficients, as

$$\boldsymbol{a}_{\mathbf{xx}} = A_h\,\widehat{\boldsymbol{a}_{\mathbf{xx}}}, \qquad a_{zz} = A_v\,\widehat{a_{zz}}, \tag{2.5a}$$

respectively. The scaling for the correlation operator and the cross component of the diffusion tensor follows:

$$\boldsymbol{\sigma}_\mathbf{x} = \sqrt{2}A_h^{1/2}\,\widehat{\boldsymbol{\sigma}_\mathbf{x}}, \qquad \sigma_z = \sqrt{2}A_v^{1/2}\,\widehat{\sigma_z}, \qquad \boldsymbol{a}_{\mathbf{x}z} = A_h^{1/2}A_v^{1/2}\,\widehat{\boldsymbol{a}_{\mathbf{x}z}}. \tag{2.5b}$$

We next recall the Rossby number (Ro), horizontal Ekman number ($\mathrm{E_h}$), vertical Ekman number ($\mathrm{E_v}$), and the aspect ratio (δ), which are defined by

$$\mathrm{Ro} = \frac{U}{f_0 L}, \qquad \mathrm{E_h} = \frac{A_h}{f_0 L^2}, \qquad \mathrm{E_v} = \frac{A_v}{f_0 H^2}, \qquad \delta = \frac{H}{L}. \tag{2.6}$$

Using these dimensionless numbers, the Itô-Stokes drift $\mathbf{v}_s$ normalized by the characteristic scales of $\mathbf{v}^\star$ scales as

$$\widetilde{\mathbf{u}}_s := \frac{\mathbf{u}_s}{U} = \frac{\mathrm{E_h}}{\mathrm{Ro}}\,\widehat{\nabla}\cdot\widehat{\boldsymbol{a}_{\mathbf{xx}}} + \frac{\mathrm{E_h}^{1/2}}{\mathrm{Ro}}\frac{\mathrm{E_v}^{1/2}}{\widehat{\delta_e}}\,\partial_{\widehat{\zeta}}\widehat{\boldsymbol{a}_{\mathbf{x}z}}, \tag{2.7a}$$

$$\widetilde{w}_s := \frac{w_s}{W} = \frac{\mathrm{E_h}^{1/2}}{\mathrm{Ro}}\mathrm{E_v}^{1/2}\,\widehat{\nabla}\cdot\widehat{\boldsymbol{a}_{\mathbf{x}z}} + \frac{1}{\mathrm{Ro}}\frac{\mathrm{E_v}}{\widehat{\delta_e}}\,\partial_{\widehat{\zeta}}\widehat{a_{zz}}. \tag{2.7b}$$

Note that $\nabla = (\partial_x, \partial_y)^T$ represents the horizontal gradient from here on.

The advection time scale $t = (L/U)\widehat{t}$ is imposed as the characteristic time scale. It is important to note that the time scale, $\widehat{t}$, is not necessarily of O(1). Discussed later, two different time scales will indeed be used to distinctly capture a stationary and a non stationary stochastic Ekman model. The variance of a (cylindrical) Brownian motion also takes the scale of time, with $B_t = (L/U)^{1/2}\,\widehat{B}_t$. Moreover, the scale of unresolved pressure noise are suggested by the geostrophic balance $f\hat{\mathbf{z}}\times\boldsymbol{\sigma}\mathrm{d}B_t \approx -\nabla \mathrm{d}P_t$, hence $P_t = \sqrt{2}(\mathrm{E_h}/\mathrm{Ro})^{1/2} f_0 L^2\,\widehat{P}_t$.

Substituting the above scalings in Eq. (2.3), the following nondimensional stochastic momentum equations is obtained:

$$\begin{aligned}
&\mathrm{Ro}\left(\mathrm{d}\widehat{\mathbf{u}} + \left(\widehat{\mathbf{u}}\cdot\widehat{\nabla} + \widehat{w}\partial_{\widehat{\zeta}}\right)\left(\widehat{\mathbf{u}}+\widetilde{\mathbf{u}}_s\right)\mathrm{d}\widehat{t}\right) + \sqrt{2}\mathrm{Ro}^{1/2}\left(\mathrm{E_h}^{1/2}\widehat{\boldsymbol{\sigma}_{\mathbf{x}}}\cdot\widehat{\nabla} + \frac{\mathrm{E_v}^{1/2}}{\widehat{\delta_e}}\widehat{\sigma}_z\partial_{\widehat{\zeta}}\right)\left(\widehat{\mathbf{u}}+\widetilde{\mathbf{u}}_s\right)\mathrm{d}\widehat{B}_t \\
&\quad = -\left(\widehat{f}\left(\widehat{\mathbf{u}}+\widetilde{\mathbf{u}}_s\right)^{\perp} + \widehat{\nabla}\widehat{p}\right)\mathrm{d}\widehat{t} - \sqrt{2}\frac{\mathrm{E_h}^{1/2}}{\mathrm{Ro}^{1/2}}\left(\widehat{f}\widehat{\boldsymbol{\sigma}_{\mathbf{x}}}^{\perp}\mathrm{d}\widehat{B}_t + \widehat{\nabla}\mathrm{d}\widehat{P}_t\right) + \mathrm{E_h}\widehat{\nabla}\cdot\left(\widehat{\boldsymbol{a}_{\mathbf{xx}}}\widehat{\nabla}\left(\widehat{\mathbf{u}}+\widetilde{\mathbf{u}}_s\right)\right)\mathrm{d}\widehat{t} \\
&\qquad + \frac{\mathrm{E_v}}{\widehat{\delta_e}^2}\partial_{\widehat{\zeta}}\left(\widehat{a_{zz}}\partial_{\widehat{\zeta}}\left(\widehat{\mathbf{u}}+\widetilde{\mathbf{u}}_s\right)\right)\mathrm{d}\widehat{t} + \mathrm{E_h}^{1/2}\frac{\mathrm{E_v}^{1/2}}{\widehat{\delta_e}}\left(\widehat{\nabla}\cdot\left(\widehat{\boldsymbol{a}_{\mathbf{x}z}}\partial_{\widehat{\zeta}}\left(\widehat{\mathbf{u}}+\widetilde{\mathbf{u}}_s\right)\right) + \partial_{\widehat{\zeta}}\left(\widehat{\boldsymbol{a}_{\mathbf{x}z}}\widehat{\nabla}\left(\widehat{\mathbf{u}}+\widetilde{\mathbf{u}}_s\right)\right)\right)\mathrm{d}\widehat{t}, \qquad (2.8a)
\end{aligned}$$

$$\begin{aligned}
&\delta^2\mathrm{Ro}\left(\mathrm{d}\widehat{w} + \left(\widehat{\mathbf{u}}\cdot\widehat{\nabla} + \widehat{w}\partial_{\widehat{\zeta}}\right)\left(\widehat{w}+\widetilde{w}_s\right)\mathrm{d}\widehat{t}\right) + \sqrt{2}\delta^2\mathrm{Ro}^{1/2}\left(\mathrm{E_h}^{1/2}\widehat{\boldsymbol{\sigma}_{\mathbf{x}}}\cdot\widehat{\nabla} + \frac{\mathrm{E_v}^{1/2}}{\widehat{\delta_e}}\widehat{\sigma}_z\partial_{\widehat{\zeta}}\right)\left(\widehat{w}+\widetilde{w}_s\right)\mathrm{d}\widehat{B}_t \\
&\quad = -\frac{1}{\widehat{\delta_e}^2}\left(\partial_{\widehat{\zeta}}\widehat{p}\mathrm{d}\widehat{t} + \sqrt{2}\frac{\mathrm{E_h}^{1/2}}{\mathrm{Ro}^{1/2}}\partial_{\widehat{\zeta}}\mathrm{d}\widehat{P}_t\right) + \delta^2\left(\mathrm{E_h}\widehat{\nabla}\cdot\left(\widehat{\boldsymbol{a}_{\mathbf{xx}}}\widehat{\nabla}\left(\widehat{w}+\widetilde{w}_s\right)\right) + \frac{\mathrm{E_v}}{\widehat{\delta_e}^2}\partial_{\widehat{\zeta}}\left(\widehat{a_{zz}}\partial_{\widehat{\zeta}}\left(\widehat{w}+\widetilde{w}_s\right)\right)\right. \\
&\qquad \left. + \mathrm{E_h}^{1/2}\frac{\mathrm{E_v}^{1/2}}{\widehat{\delta_e}}\left(\widehat{\nabla}\cdot\left(\widehat{\boldsymbol{a}_{\mathbf{x}z}}\partial_{\widehat{\zeta}}\left(\widehat{w}+\widetilde{w}_s\right)\right) + \partial_{\widehat{\zeta}}\left(\widehat{\boldsymbol{a}_{\mathbf{x}z}}\widehat{\nabla}\left(\widehat{w}+\widetilde{w}_s\right)\right)\right)\right)\mathrm{d}\widehat{t}, \qquad (2.8b)
\end{aligned}$$

where $\mathbf{u}^{\perp} = (-v, u)^T$. To further derive the equation of motions in the Ekman boundary layer, we make the following assumptions regarding the dimensionless numbers:

$$\mathrm{Ro} \ll 1, \quad \delta \ll 1, \quad \widehat{\delta_e} \sim \mathrm{E_v}^{1/2}, \quad \mathrm{E_h}^{1/2} \sim \mathrm{Ro}. \qquad (2.9)$$

A small Rossby number mainly neglects the nonlinear advection terms, and a small aspect ratio ensures hydrostatic balance in the vertical. The third assumption sets the vertical friction to be as large as the Coriolis force in the boundary layer, even though the Ekman number remains small in general. The last assumption emerges from the ratio of horizontal friction to inertial acceleration $\mathrm{E_h}/\mathrm{Ro} = 1/\mathrm{Re}$, where $\mathrm{Re} = UL/A_h$ is the Reynolds number of the interior flow. In most cases of

geophysical interest the Reynolds number is quite large (Pedlosky 1990, chap. 4). In particular, we choose $1/\mathrm{Re} \sim \mathrm{Ro}$ here. Using the above assumptions, the previous nondimensional momentum equations reduce to

$$\begin{aligned}\mathrm{Ro}\,\mathrm{d}\widehat{\mathbf{u}} = &\left(-\widehat{f}\big(\widehat{\mathbf{u}} + \partial_{\widehat{\zeta}}\widehat{\boldsymbol{a}_{\mathbf{x}z}}\big)^{\perp} - \widehat{\nabla}\widehat{p} + \partial_{\widehat{\zeta}}\Big(\widehat{a_{zz}}\partial_{\widehat{\zeta}}\big(\widehat{\mathbf{u}} + \partial_{\widehat{\zeta}}\widehat{\boldsymbol{a}_{\mathbf{x}z}}\big)\Big) + O(\mathrm{Ro})\right)\mathrm{d}\widehat{t} \\ &- \sqrt{2}\mathrm{Ro}^{1/2}\left(\Big(\widehat{\sigma_z}\partial_{\widehat{\zeta}}\big(\widehat{\mathbf{u}} + \partial_{\widehat{\zeta}}\widehat{\boldsymbol{a}_{\mathbf{x}z}}\big) + \widehat{f}\,\widehat{\boldsymbol{\sigma}_{\mathbf{x}}}^{\perp}\Big)\mathrm{d}\widehat{B}_t + \widehat{\nabla}\mathrm{d}\widehat{P}_t\right) + O(\mathrm{Ro})\mathrm{d}\widehat{B}_t, \end{aligned} \tag{2.10a}$$

$$\delta^2\mathrm{Ro}\,\mathrm{d}\widehat{w} = \left(-\frac{1}{\widehat{\delta_e}^{\,2}}\partial_{\widehat{\zeta}}\widehat{p} + O\big(\delta^2\big)\right)\mathrm{d}\widehat{t} - \sqrt{2}\frac{\mathrm{Ro}^{1/2}}{\widehat{\delta_e}^{\,2}}\partial_{\widehat{\zeta}}\mathrm{d}\widehat{P}_t + O\big(\delta^2\big)\mathrm{d}\widehat{B}_t. \tag{2.10b}$$

In the following sections, a steady model with random coefficients is first derived and then a time-dependent random model, according to two different time scales.

c. Steady Ekman-Stokes model with random coefficients

To derive a steady solution, an intermediate time scale $\widehat{t} = O(1)$ is considered. The temporal variation of horizontal momentum is neglected, Eq. (2.10a) can thus be split into a prognostic equation of O(1) in terms of "$\mathrm{d}\widehat{t}$" and a diagnostic equation of $\mathrm{O}(\mathrm{Ro}^{1/2})$ in terms of "$\mathrm{d}\widehat{B}_t$". This splitting, based on physical scaling arguments, is also ensured from a mathematical point of view, by the canonical decomposition of semi-martingale (Le Gall 2016, chap. 4). Similarly, the vertical momentum (2.10b) reduces to two hydrostratic balances for the resolved and unresolved scales. It comes:

$$\widehat{f}(\widehat{\mathbf{u}} + \widehat{\mathbf{u}}_s)^{\perp} = -\widehat{\nabla}\widehat{p} + \partial_{\widehat{\zeta}}\big(\widehat{a_{zz}}\partial_{\widehat{\zeta}}(\widehat{\mathbf{u}} + \widehat{\mathbf{u}}_s)\big), \quad \widehat{\mathbf{u}}_s = \partial_{\widehat{\zeta}}\widehat{\boldsymbol{a}_{\mathbf{x}z}}, \tag{2.11a}$$

$$\big(\widehat{f}\,\widehat{\boldsymbol{\sigma}_{\mathbf{x}}}^{\perp} - \widehat{\sigma_z}\partial_{\widehat{\zeta}}(\widehat{\mathbf{u}} + \widehat{\mathbf{u}}_s)\big)\mathrm{d}\widehat{B}_t = -\widehat{\nabla}\mathrm{d}\widehat{P}_t, \tag{2.11b}$$

$$\partial_{\widehat{\zeta}}\widehat{p} = 0, \quad \partial_{\widehat{\zeta}}\mathrm{d}\widehat{P}_t = 0. \tag{2.11c}$$

Following Vallis (2017, chap. 5), considering $\widehat{p}$ independent of z facilitates the separation betwenn pressure-driven interior geostrophic motions and boundary layer ageostrophic motions. Let $\widehat{\mathbf{u}} = \widehat{\mathbf{u}}_g + \widehat{\mathbf{u}}_e$ and $\widehat{p} = \widehat{p}_g + \widehat{p}_e$, where the Ekman layer corrections, denoted with a subscript e, are negligible away from the boundary layer. Combining with the hydrostasy, we have $\widehat{p}_e = 0$ everywhere, hence there is no boundary layer in the pressure field. Restoring the dimensions, the ageostrophic velocity

in the Ekman layer thus satisfies

$$f(\mathbf{u}_e+\mathbf{u}_s)^{\perp}=\partial_z\big(a_{zz}\partial_z(\mathbf{u}_e+\mathbf{u}_s)\big),\qquad \mathbf{u}_s=\partial_z\boldsymbol{a}_{\mathbf{x}z}. \tag{2.12}$$

The resulting horizontal Itô-Stokes drift in this Ekman boundary layer is given by the vertical derivative of the co-variation process ($\boldsymbol{a}_{\mathbf{x}z}$) between the horizontal and vertical components of the unresolved motions. The previous vectorial equations can be rewritten as a scalar equation for the complex velocity $\mathbf{u}=u+iv$. Together with classical boundary conditions for the momentum flux, the steady Ekman-Stokes model reads:

$$\partial_z(a_{zz}\partial_z\mathbf{u}_e)-if\mathbf{u}_e=if\mathbf{u}_s-\partial_z(a_{zz}\partial_z\mathbf{u}_s), \tag{2.13a}$$

$$\rho_o a_{zz}\partial_z\mathbf{u}_e|_{z=0}=\boldsymbol{\tau}_w,\qquad \rho_o a_{zz}\partial_z\mathbf{u}_e|_{z=-H}=0, \tag{2.13b}$$

where $\boldsymbol{\tau}_w$ denotes the surface wind stress. In the general case, this elliptic partial differential equation (PDE) includes random coefficients such as the diffusion tensor $\boldsymbol{a}$, the Itô-Stokes drift $\mathbf{u}_s$, and the wind stress $\boldsymbol{\tau}_w$. It is important to note that the derived formulation (2.13) incorporates the vertical diffusive mixing effect of the Itô-Stokes drift, and represents a generalization of the classical steady Ekman model with Coriolis-Stokes force.

Following the method proposed by Wenegrat and McPhaden (2016b), an approximated analytical solution can be proposed for (2.13). To that purpose, we first vertically differentiate (2.13a) and then multiply by $\rho_o a_{zz}$ to form an equation for the Ekman current stress $\boldsymbol{\tau}_e=\rho_o a_{zz}\partial_z\mathbf{u}_e$, which reads:

$$(a_{zz}\partial^2_{zz}-if)\boldsymbol{\tau}_e=-(a_{zz}\partial^2_{zz}-if)\boldsymbol{\tau}_s, \tag{2.14a}$$

$$\boldsymbol{\tau}_e(0)=\boldsymbol{\tau}_w,\qquad \boldsymbol{\tau}_e(-H)=0. \tag{2.14b}$$

Similarly, $\boldsymbol{\tau}_s=\rho_o a_{zz}\partial_z\mathbf{u}_s$ represents the derived Itô-Stokes stress. Wenegrat and McPhaden (2016b) propose solving their generalized Ekman model, which shares the same left-hand side differential operator with Eq. (2.14a) but with different right-hind side forces, by initially approximating a solution to the homogeneous equation using the Wentzel-Kramer-Brillouin (WKB) method. Then, the authors solve for the inhomogeneous solution using the method of variation of parameters.

Precisely following their detailed derivation to solve our boundary value problem (2.14), the full solution of Ekman stress is given by

$$\boldsymbol{\tau}_e(z) = \boldsymbol{\tau}_w \left(\frac{a_{zz}(z)}{a_{zz}(0)}\right)^{1/4} \frac{\sinh\big(\theta(z)\big)}{\sinh\big(\theta(0)\big)} + \int_{-H}^{0} G(z,\zeta)\left(\big(if a_{zz}^{-1} - \partial_{zz}^2\big)\boldsymbol{\tau}_s\right)(\zeta)\,\mathrm{d}\zeta, \tag{2.15a}$$

$$\theta(z) = \sqrt{if}\int_{-H}^{z} a_{zz}^{-1/2}(\zeta)\,\mathrm{d}\zeta. \tag{2.15b}$$

Here, G denotes a symmetric Green function defined by

$$G(z,\zeta) = \frac{a_{zz}^{1/4}(z)a_{zz}^{1/4}(\zeta)}{\sqrt{if}\sinh\big(\theta(0)\big)} g(z,\zeta), \qquad g(z,\zeta) = \begin{cases} \sinh\big(\theta(z)\big)\sinh\big(\theta(\zeta)-\theta(0)\big) & \text{if } \zeta > z \\ \sinh\big(\theta(\zeta)\big)\sinh\big(\theta(z)-\theta(0)\big) & \text{if } \zeta < z \end{cases}. \tag{2.15c}$$

The accuracy of the WKB approximate solution has been further discussed in Wenegrat and McPhaden (2016b), to generally show small errors for small vertical Ekman number ($\mathrm{E_v}$). Once this Ekman stress is found, the Ekman current solution satisfying (2.13) can be recovered by

$$\mathbf{u}_e = -\frac{i}{\rho_o f}\partial_z(\boldsymbol{\tau}_e + \boldsymbol{\tau}_s) - \mathbf{u}_s. \tag{2.16}$$

Integrating this relation vertically, a modified relation for the Ekman transport, $\mathbf{T}_e = \int_{-H}^{0}\mathbf{u}_e(z)\,\mathrm{d}z$ reads:

$$\mathbf{T}_e = -\frac{i}{\rho_0 f}\big(\boldsymbol{\tau}_w + \boldsymbol{\tau}_s^0\big) - \mathbf{T}_s. \tag{2.17}$$

It shows that the Ekman transport $\mathbf{T}_e$ is modified by both the surface Itô-Stokes stress $\boldsymbol{\tau}_s^0 := \boldsymbol{\tau}_s(0)$ and the Itô-Stokes transport $\mathbf{T}_s = \int_{-H}^{0}\mathbf{u}_s(z)\,\mathrm{d}z$. Nevertheless, the Ekman-Stokes transport $\mathbf{T}_e + \mathbf{T}_s$ is rotated 90° from the left of the effective surface stress $\boldsymbol{\tau}_w + \boldsymbol{\tau}_s^0$, hence satisfies the classical integral relation. Moreover, the vertical velocity induced by the Ekman layer, usually referred to as the *Ekman pumping*, can be derived by integrating the continuity equation (2.2c) for the ageostrophic component, namely

$$w_e(-H) = \frac{1}{\rho_o f}\nabla\times\big(\boldsymbol{\tau}_w + \boldsymbol{\tau}_s^0\big) - \nabla\cdot\mathbf{T}_s. \tag{2.18}$$

Accordingly, the Ekman pumping is now modified by both the curl of the surface Itô-Stokes stress and the horizontal divergence of the Itô-Stokes transport. Through the Itô-Stokes drift, it

incorporates the statistical effect of the inhomogeneity of the small-scale velocity component. It absorbs wavy motions, but also other physical processes affecting small-scale velocity fluctuations, as well as the effect of its vertical mixing. This relation can be beneficial for numerical ocean models at coarse resolution, providing a means to parameterize the Ekman-Stokes layer without explicitly solving the Ekman current (2.14) due to limited vertical resolution.

d. Time-dependent stochastic Ekman-Stokes model

In this case, a fast time scale is considered by applying a change of time coordinates (Crowe and Taylor 2018), such that $\widehat{\tau} = \widehat{t}/\mathrm{Ro}$, and hence $\widehat{B_\tau} = \widehat{B}_t/\mathrm{Ro}^{1/2}$. Therefore, equations (2.10a) and (2.10b) boils down to

$$\begin{aligned} \mathrm{d}\widehat{\mathbf{u}} = &\left(-\widehat{f}(\widehat{\mathbf{u}}+\widehat{\mathbf{u}}_s)^\perp - \widehat{\nabla}\widehat{p} + \partial_{\widehat{\zeta}}\left(\widehat{a_{zz}}\partial_{\widehat{\zeta}}(\widehat{\mathbf{u}}+\widehat{\mathbf{u}}_s)\right)\right)\mathrm{d}\widehat{\tau} \\ &- \sqrt{2}\left(\widehat{f}\widehat{\boldsymbol{\sigma}_{\mathbf{x}}}^\perp + \widehat{\sigma}_z\partial_{\widehat{\zeta}}(\widehat{\mathbf{u}}+\widehat{\mathbf{u}}_s)\right)\mathrm{d}\widehat{B_\tau} - \sqrt{2}\widehat{\nabla}\mathrm{d}\widehat{P_\tau}, \end{aligned} \tag{2.19a}$$

$$\partial_{\widehat{\zeta}}\widehat{p} = 0, \qquad \partial_{\widehat{\zeta}}\mathrm{d}\widehat{P_\tau} = 0. \tag{2.19b}$$

Unlike the steady case, the contributions of the "$\mathrm{d}\widehat{t}$" and "$\mathrm{d}\widehat{B}_t$" terms on the momentum evolution can no longer be separated. Both terms have exactly the same scales. Again separating the pressure-driven geostrophic motions, the wind-driven ageostrophic motions in the Ekman layer satisfy the following dimensional SPDE under complex notations:

$$\mathrm{d}\mathbf{u}_e = \Big(-if(\mathbf{u}_e+\mathbf{u}_s) + \partial_z\left(a_{zz}\partial_z(\mathbf{u}_e+\mathbf{u}_s)\right)\Big)\mathrm{d}t - (if\boldsymbol{\sigma}_{\mathbf{x}} + \sigma_z\partial_z(\mathbf{u}_e+\mathbf{u}_s))\,\mathrm{d}B_t, \tag{2.20a}$$

$$\rho_o a_{zz}\partial_z\mathbf{u}_e|_{z=0} = \boldsymbol{\tau}_w, \qquad \rho_o a_{zz}\partial_z\mathbf{u}_e|_{z=-H} = 0. \tag{2.20b}$$

This stochastic formulation extends the classical time-dependent Ekman-Stokes model (McWilliams et al. 1997), incorporating the vertical unresolved advective process of Ekman current, the random unresolved Coriolis force, and both the diffusive and advective vertical mixing effects of the Itô-Stokes drift.

Finding analytical expression of strong (pathwise) solutions to a SPDE with multiplicative noises is extremely challenging. A general representation of solutions can be used to study the well-posedness of the proposed SPDE. For instance, the notion of mild solutions (see Da Prato and

Zabczyk 2014, chap. 6) can be defined as a temporal convolution of nonlinear/force and noise terms by an analytical semigroup generated by the linear operator of the SPDE. Additionally, a general representation for the statistical moments of a solution to the SPDE can be formulated based on Wiener chaos expansion (Mikulevicius and Rozovskii 1998, 2004). However, analytically solving the expansion coefficients corresponding to the solutions of a very high-dimensional system of deterministic PDEs remains difficult. Instead, in Section 3, the statistical moments for solutions of the SPDE (2.20), incorporating other random parameters are investigated through numerical simulations, using the Monte Carlo method.

First, let us exemplify important integral properties of the conditional mean solution. Assuming the random correlation operator $\boldsymbol{\sigma}$ and the cylindrical Brownian motion B are independent, and taking the expectation of Eq. (2.20a) with respect to the conditional probability distribution of $\boldsymbol{\sigma}$, we deduce the following PDE for $\mathbb{E}^{\sigma}[\mathbf{u}_e] := \mathbb{E}[\mathbf{u}_e|\boldsymbol{\sigma}]$:

$$\partial_t \mathbb{E}^{\sigma}[\mathbf{u}_e] = -if\left(\mathbb{E}^{\sigma}[\mathbf{u}_e] + \mathbf{u}_s\right) + \partial_z\left(a_{zz}\partial_z(\mathbb{E}^{\sigma}[\mathbf{u}_e] + \mathbf{u}_s)\right). \tag{2.21}$$

This resulting PDE remains random, with $\mathbb{E}^{\sigma}[\mathbf{u}]$ a function of $\boldsymbol{\sigma}$ which is random. Integrating vertically, it comes an initial value problem with random parameters for the conditional mean Ekman transport, $\mathbb{E}^{\sigma}[\mathbf{T}_e](t) = \int_0^{-H} \mathbb{E}^{\sigma}[\mathbf{u}_e](z,t)\,\mathrm{d}z$, which reads

$$\frac{\mathrm{d}}{\mathrm{d}t}\mathbb{E}^{\sigma}[\mathbf{T}_e] = -if\mathbb{E}^{\sigma}[\mathbf{T}_e] + \frac{1}{\rho_o}\left(\boldsymbol{\tau}_w + \boldsymbol{\tau}_s^0\right) - if\mathbf{T}_s. \tag{2.22a}$$

Its solution is given by

$$\mathbb{E}^{\sigma}[\mathbf{T}_e](t) = e^{-ift}\mathbb{E}^{\sigma}[\mathbf{T}_e](0) + \frac{1}{\rho_o}\int_0^t e^{-if(t-r)}\left(\boldsymbol{\tau}_w + \boldsymbol{\tau}_s^0\right)(r)\,\mathrm{d}r - \mathbf{T}_s\left(1 - e^{-ift}\right). \tag{2.22b}$$

We recall that the Itô-Stokes drift $\mathbf{u}_s$ is assumed to be quasi-stationary (hence $\mathbf{T}_s$ is also), whereas the wind stress $\boldsymbol{\tau}_w$ and the vertical diffusion coefficient a_{zz} are possibly time-dependent (and consequently $\boldsymbol{\tau}_s^0 = a_{zz}\partial_z\mathbf{u}_s|_{z=0}$ as well). Taking the divergence of the previous equation, we obtain

the following solution for the conditional mean Ekman pumping at the lower boundary:

$$\mathbb{E}^{\sigma}[w_e](t) = \cos(ft)\mathbb{E}^{\sigma}[w_e](0) + \big(\cos(ft)+1\big)\nabla\cdot\mathbf{T}_s + \frac{1}{\rho_o}\int_0^t \sin\big(f(t-r)\big)\nabla\times\big(\boldsymbol{\tau}_w+\boldsymbol{\tau}_s^0\big)(r)\,\mathrm{d}r$$
$$+\cos(ft)\nabla\times\big(\mathbb{E}^{\sigma}[\mathbf{T}_e](0)+\mathbf{T}_s\big) + \frac{1}{\rho_o}\int_0^t \sin\big(f(t-r)\big)\nabla\cdot\big(\boldsymbol{\tau}_w+\boldsymbol{\tau}_s^0\big)(r)\,\mathrm{d}r. \qquad (2.23)$$

The Ekman pumping resulting from the unsteady Ekman-Stokes boundary layer depends on both the divergence and curl components of the initial Ekman transport, the steady Itô-Stokes transport, and the time-dependent effective surface stress. Note again that the additional terms compared to the classical case are related to the surface Itô-Stokes stress $\boldsymbol{\tau}_s^0$.

e. Consistent physical parameterization for uncertainty representation

In most of our previous works (Bauer et al. 2020; Resseguier et al. 2021; Brecht et al. 2021; Li et al. 2023a; Tucciarone et al. 2024), the noise was parameterized through a spectral decomposition of the correlation operator $\boldsymbol{\sigma}$. Stationary as well as time-evolving representations, performed with proper orthogonal decomposition, dynamic mode decomposition, wavelet basis, or auto-similarity assumptions, have been used for the definition of data-driven or model-based noises. The corresponding diffusion tensor $\boldsymbol{a}$ and the resulting Itô-Stokes drift $\mathbf{v}_s$, defined in (2.2b), are then directly obtained from the noise basis function definition. In the present work, an opposite approach is somehow considered: given specific physical parameterizations for the vertical diffusion coefficient a_{zz} and the horizontal Stokes drift $\mathbf{u}_s$, objectives are to derive the corresponding vertical and horizontal components of the unresolved random flow component $\boldsymbol{\sigma}\mathrm{d}B_t$. Besides, the randomness of the correlation operator $\boldsymbol{\sigma}$, which acts as an additional random source, is induced by a parameterized wind process and a steady distribution of the surface wave direction. For the sake of simplicity and without loss of generality, we present the formulation for one-dimensional boundary layer models in the following sections.

1) Random wind and wind stress

We adopt here the random wind parameterization proposed by McWilliams and Huckle (2006). The total wind $\mathbf{u}_a$ is decomposed into its time average $\overline{\mathbf{u}_a}$ and fluctuations $\mathbf{u}_a'$. Each of the fluctuating

wind components is modeled as an independent Ornstein-Uhlenbeck (OU) process,

$$\mathrm{d}\mathbf{u}_a' = -\frac{1}{T_a}\mathbf{u}_a' \,\mathrm{d}t + \sqrt{\frac{2}{T_a}}\Sigma_a \,\mathrm{d}\mathbf{W}_t, \tag{2.24}$$

where T_a denotes the memory time, Σ_a stands for the standard deviation of $\mathbf{u}_a'$, both conditioning the transient behavior of the OU process, and $\mathbf{W}_t = W_t^x + iW_t^y$ with W_t^x and W_t^y being two independent standard Brownian motions. These two Brownian motions are assumed mutually independent from the cylindrical Brownian motion involved in the definition of the unresolved current component $\boldsymbol{\sigma}\,\mathrm{d}B_t$, as they are attached to processes originating from different physical medias (atmosphere and ocean). This independence also ensures that the conditional mean Ekman transport solution discussed in the previous section remains valid.

The ocean surface wind stress $\boldsymbol{\tau}_w$ follows the classical bulk formula, quadratic with respect to the total wind $\mathbf{u}_a$:

$$\boldsymbol{\tau}_w = C_D \rho_a |\mathbf{u}_a| \mathbf{u}_a = \rho_o u_*^2 e^{i\theta_*}, \tag{2.25}$$

where C_D is the air-sea drag coefficient, ρ_a is the air density, u_* is the friction velocity, and θ_* denotes the angular direction of the wind stress. It is important to note that the resulting parameters $\boldsymbol{\tau}_w$, u_*, and θ_* are random, leading to additional randomness in other parameters as discussed subsequently.

2) Vertical diffusion coefficient

For the vertical diffusion, the well-established *K-Profile Parameterization* (KPP) model (Large et al. 1994; McWilliams and Huckle 2006) is considered to represent the vertical eddy viscosity a_{zz} within the turbulent surface boundary layer. This parameterization is nonlocal and adheres the predictions of Monin-Obukhov similarity theory along with other extensions (Fox-Kemper et al. 2022). It is formulated as follows:

$$a_{zz}(z) = c_1 u_* h G(\zeta), \qquad \zeta = -z/h, \qquad h = c_2 \frac{u_*}{f}, \tag{2.26a}$$

where c_1 and c_2 are constants that determine the amplitude and shear of a_{zz}, h is the boundary layer depth, and G is a smooth function of the normalized depth ζ. We adopt a specific version of

G proposed by McWilliams and Huckle (2006), which includes an additional regularization term very near the ocean surface:

$$G(\zeta) = \zeta(1-\zeta)^2 + \mathrm{H}(\zeta_0 - \zeta)\frac{(\zeta-\zeta_0)^2}{2\zeta_0}, \tag{2.26b}$$

where H denotes the Heaviside step function. This KPP model is illustrated in Fig. 1 (a). Analyzed by McWilliams and Huckle (2006) in physical terms, the final regularization term represents an extra mixing phenomenon occurring within the oceanic boundary layer, possibly taking into account surface gravity wave breaking and mixing confined within a shallow layer with a thickness of $\zeta_0 h$ (where ζ_0 is assumed to be sufficiently small). Since u_* is random, both the diffusion coefficient a_{zz} and the boundary layer depth h are also random. Note that more complex schemes based on second-moment closure (Mellor and Yamada 1982; Harcourt 2013, 2015) could be further investigated following a similar construction.

3) Stokes drift and wave stress

Consider a steady, monochromatic, deep-water wave with surface elevation, to leading order in wave steepness, expressed as $\eta = \alpha\cos(kx - \omega t)$, where α is the wave amplitude, k is the horizontal wavenumber, $\omega = (gk)^{1/2}$ is the angular frequency satisfying the deep-water dispersion relation. The corresponding horizontal components of the Stokes drift are approximately given by (Phillips 1977, chap. 4)

$$\mathbf{u}_s(z) = U_0 e^{2kz} e^{i\theta_s}, \tag{2.27a}$$

where $U_0 = \omega k \alpha^2$ represents the Stokes drift magnitude, and θ_s is the wave propagation direction. This Stokes drift velocity is nonlinear with respect to the wave amplitude and decays exponentially with depth from the ocean surface, Fig. 1 (b).

In reality, surface gravity waves exhibit a broad-band spectrum, leading to a more complex vertical profile for the Stokes drift (Huang 1971; Jenkins 1989). The randomness inherent in the KPP model results in the derived wave stress amplitude $\boldsymbol{\tau}_s = a_{zz}\partial_z \mathbf{u}_s$ being equally random. To capture the uncertainty in the wave propagation direction, we parameterize it using a Gaussian distribution:

$$\theta_s \sim \mathcal{N}(\Theta_s, \Sigma_s^2), \tag{2.27b}$$

where Θ_s and Σ_s denote its mean and standard deviation, respectively. Note that the wave stress $\boldsymbol{\tau}_s$ is consequently random but non-Gaussian.

4) Unresolved random flow

Given a diffusion coefficient a_{zz} and a Stokes drift $\mathbf{u}_s$, the vertical and horizontal components of the unresolved noise flow are specified by the following projection formulation:

$$\widetilde{\sigma}_z \, \mathrm{d}B_t = \sqrt{2} \sum_n \left\langle a_{zz}^{1/2}, e_n \right\rangle e_n \, \mathrm{d}\beta_n, \tag{2.28a}$$

$$\widetilde{\boldsymbol{\sigma}}_{\mathbf{x}} \, \mathrm{d}B_t = \sqrt{2} \sum_n \left(\left\langle a_{zz}^{-1/2} U_s, e_n \right\rangle + i \left\langle a_{zz}^{-1/2} V_s, e_n \right\rangle \right) e_n \, \mathrm{d}\beta_n, \tag{2.28b}$$

$$\mathbf{U}_s = \int_{-H}^{z} \mathbf{u}_s(\zeta) \, \mathrm{d}\zeta = U_s + i V_s, \tag{2.28c}$$

where $\{e_n\}$ is a set of orthogonal basis functions of the real-valued Hilbert space $L^2([-H,0],\mathbb{R})$ equipped with the inner product $\langle f, g \rangle = \int_{-H}^{0} f(z) g(z) \, \mathrm{d}z$, $\{\beta_n\}$ is a set of independent standard Brownian motions, and $\mathbf{U}_s$ denotes antiderivative of Stokes drift. This latter reduces to $\mathbf{u}_s/(2k)$ for the Stokes drift velocity corresponding to the monochromatic deep-water wave as defined in (2.27a). Better approximations of $\mathbf{U}_s$ could be further explored for more accurate expression of $\mathbf{u}_s$. Note that Eq. (2.28b) is only defined within the support of the function a_{zz}, and we simply impose zero horizontal noise $\boldsymbol{\sigma}_{\mathbf{x}} \, \mathrm{d}B_t$ outside the support.

The diffusion processes corresponding to the previous noise formulation are then given by

$$\widetilde{a}_{zz} = \sum_n \left\langle a_{zz}^{1/2}, e_n \right\rangle^2 e_n^2, \quad \widetilde{\boldsymbol{a}}_{\mathbf{x}z} = \sum_n \left\langle a_{zz}^{1/2}, e_n \right\rangle \left(\left\langle a_{zz}^{-1/2} U_s, e_n \right\rangle + i \left\langle a_{zz}^{-1/2} V_s, e_n \right\rangle \right) e_n^2. \tag{2.29}$$

Parseval's theorem shows that the reconstructed diffusion coefficients are globally identified with the vertical viscosity and the antiderivative of Stokes drift:

$$\int_{-H}^{0} \widetilde{a}_{zz}(z) \, \mathrm{d}z = \int_{-H}^{0} a_{zz}(z) \, \mathrm{d}z, \quad \int_{-H}^{0} \widetilde{\boldsymbol{a}}_{\mathbf{x}z}(z) \, \mathrm{d}z = \int_{-H}^{0} \mathbf{U}_s(z) \, \mathrm{d}z. \tag{2.30a}$$

With the assumption that the basis functions $\{e_n\}$ are localized, meaning that each of them is significant only in a small localized region of the domain with negligible overlapping support,

Parseval's theorem is valid almost pointwise, and we obtain the approximation:

$$\widetilde{a}_{zz}(z) \approx a_{zz}(z), \qquad \widetilde{\boldsymbol{a}}_{\mathbf{x}z}(z) \approx \mathbf{U}_s(z). \tag{2.30b}$$

Consequently, the resulting Itô-Stokes drift $\widetilde{\mathbf{u}}_s = \partial_z \widetilde{\boldsymbol{a}}_{\mathbf{x}z}$ approximates the given Stokes drift $\mathbf{u}_s$.

Although the noise is specified through simple models of diffusion (KPP) and Itô-Stokes statistical drift (Stokes drift of monochromatic waves), its normal distribution is not trivial to specify. It depends nonlinearly on random parameters. Its response to small variations of the parameters is not straightforward to infer. Furthermore, the resulting noise acts as both an additive noise and an advection process (transport noise), which is non-Gaussian.

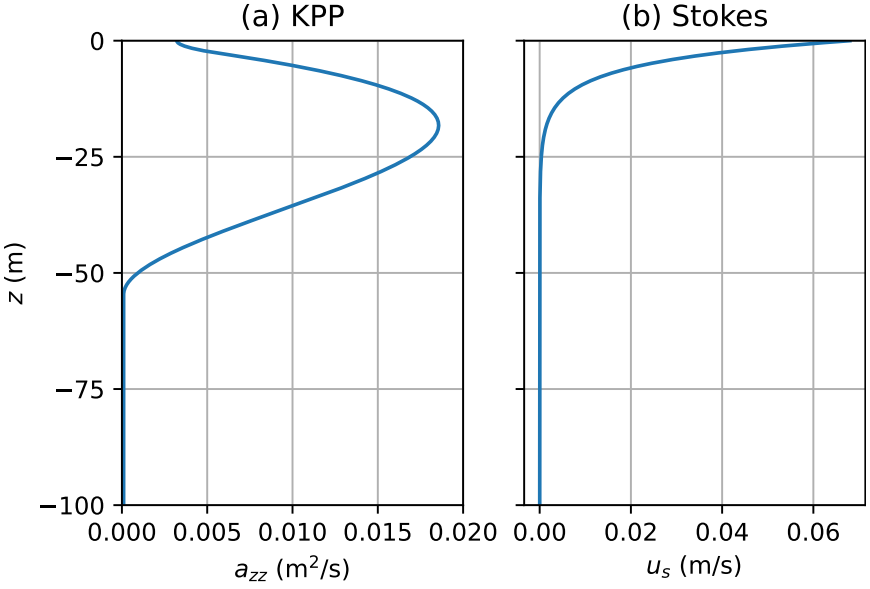

FIG. 1. Illustration depicting the K-Profile Parameterization (KPP) viscosity coefficient alongside a zonal Stokes drift profile.

3. Statistical analyses

In this section, statistical properties of the proposed time-dependent stochastic Ekman-Stokes model (2.20) are investigated. Large-ensemble simulations are performed using a Monte Carlo method. The numerical schemes employed for simulating the SPDE, as well as for the Markovian wind stress process, are detailed in Appendix A.

The proposed model is first compared to a traditional benchmark model that does not account for stochastic transports and wave-mixing effects. Subsequently, we conduct comparative studies involving various wind and wave parameters.

a. Comparison with a benchmark model

The ensemble statistics derived from the proposed parameterized SPDE (2.20), referred to as *p-SPDE*, are first compared with those of a benchmark model (McWilliams et al. 1997) solely considering the Coriolis-Stokes force, driven by the parameterized PDE, designated as *p-PDE*:

$$\partial_t \mathbf{u}_e + if(\mathbf{u}_e + \mathbf{u}_s) = \partial_z(a_{zz}\partial_z \mathbf{u}_e). \tag{3.1}$$

This comparison is conducted under identical initial and boundary conditions. The common parameters between both simulations are listed in Table 1. Specifically, we assume the mean direction for both wind and wave to be zonal. It is noteworthy that the selected surface wave amplitude $\alpha = 0.8$ m and wavelength $\lambda = 60$ m (or wavenumber $k = 2\pi/\lambda \approx 1.05$ m^{-1}) proposed by McWilliams et al. (1997) imply a Stokes drift magnitude $U_0 \approx 0.068$ m s^{-1} and a Stokes layer depth $h_s = 1/(2k) \approx 4.775$ m. Additionally, it is pertinent to mention that the transient wind level in this scenario is set to be equal to the mean wind level ($\Sigma_a = \overline{u}_a = 5$ m s^{-1}) to emphasize the rectification of the Ekman layer (McWilliams and Huckle 2006).

Under these parameters, the probability density functions (PDFs) for the surface forcings (wind, wind stress, and derived wave stress in the p-SPDE), after reaching the statistically stationary states, are shown Fig. 2. These bivariate PDFs are estimated from the ensemble vector fields by a non-parametric Kernel Density Estimation (KDE) method using Gaussian kernels. As anticipated, Fig.2 (a) illustrates the Gaussian nature of the wind vector $\mathbf{u}_a$ with uncorrelated components, implying independence in the Gaussian case. However, the non-linearity of the bulk formula (2.25) results in a non-Gaussian distribution for the wind stress $\boldsymbol{\tau}_w$. Fig.2 (b) reveals that the distribution is skewed towards the left of the mean value. Additionally, Fig. 2 (c) highlights a significant bias in the distribution of the surface wave stress vector $\boldsymbol{\tau}_s^0 = \rho_o a_{zz}\partial_z \mathbf{u}_s|_{z=0}$ derived in the p-SPDE (2.20).

With these parameterized distributions, we proceed to the analysis of the response of the two random models. Fig. 3 compares the ensemble mean and spread of the Ekman velocity components,

TABLE 1. Common parameters used for simulations.

Parameters	Value	Description
f	0.73×10^{-4} s^{-1}	Coriolis frequency
ρ_o	1000 kg m^{-3}	Water density
ρ_a	1 kg m^{-3}	Air density
C_D	1.3×10^{-3}	Air-sea drag coefficient
$\overline{\mathbf{u}}_a$	5 m s^{-1}	Mean wind speed
Σ_a	5 m s^{-1}	Standard deviation of transient wind
T_a	1 day	Memory time of fluctuation wind
c_1	0.4	von Kármán constant
c_2	0.7	Constant in boundary layer depth
ζ_0	0.05	Normalized depth of shallow layer
κ_b	10^{-4} m^2 s^{-1}	Background uniform viscosity
α	0.8 m	Surface wave amplitude
k	1.05 m^{-1}	Wavenumber of Stokes drift
Θ_s	0°	Stokes drift mean direction angle
Σ_s	5°	Standard deviation of wave angles
H	256 m	Vertical domain depth
N_z	512	Number of Chebyshev points
N_r	1000	Number of random realizations
Δt	30 min	Timestep

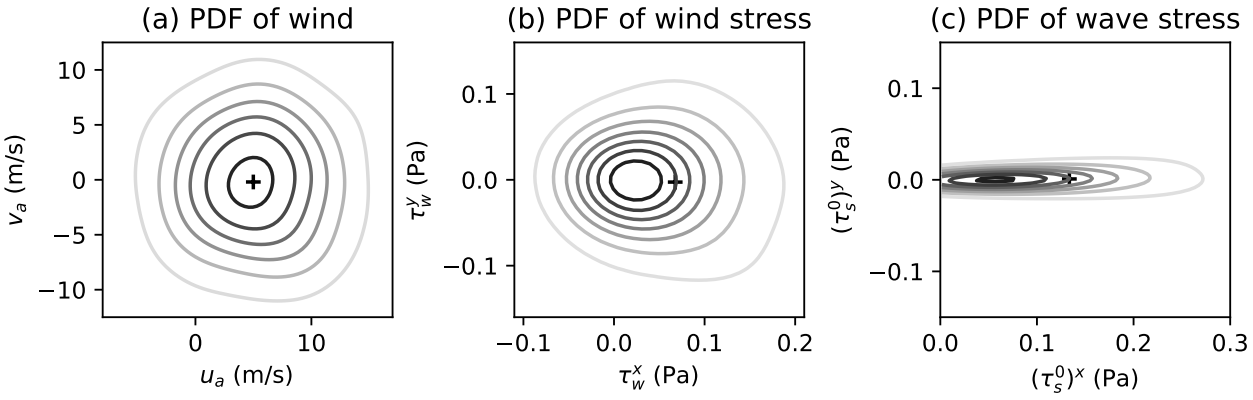

FIG. 2. Contour plots of probability density function for (a) the wind $\mathbf{u}_a$, (b) the wind stress $\boldsymbol{\tau}_w$ and (c) the derived surface wave stress $\boldsymbol{\tau}_s^0$ after 30 days. In each panel, darker-colored contours represent higher density and + marks indicate the ensemble mean.

along with the ensemble mean kinetic energy (MKE, defined as the energy of the mean solution) and eddy kinetic energy (EKE, defined as the sum of variance components) densities. Additionally, we examine the Pearson correlation coefficient (PCC) for the Ekman velocity components. Compared

to the p-PDE, the p-SPDE considering the additional wave mixing and stochastic transport effects produces a smoother profile of mean Ekman velocities with a higher spread over depth, indicating greater uncertainty (Fig. 3 (a,b)). This smoother mean profile is due to the diffusion brought by the Itô-Stokes drift.

Additionally, the p-SPDE yields higher MKE and EKE with larger differences between them (Fig. 3 (c)), and stronger correlation between the zonal and meridional components (Fig. 3 (d)) throughout the depth. These differences are particularly pronounced near the ocean surface. Note that both models exhibit higher EKE than MKE throughout the depth, a negative correlation in the upper 50 m and a positive correlation in the subsequent 100 m.

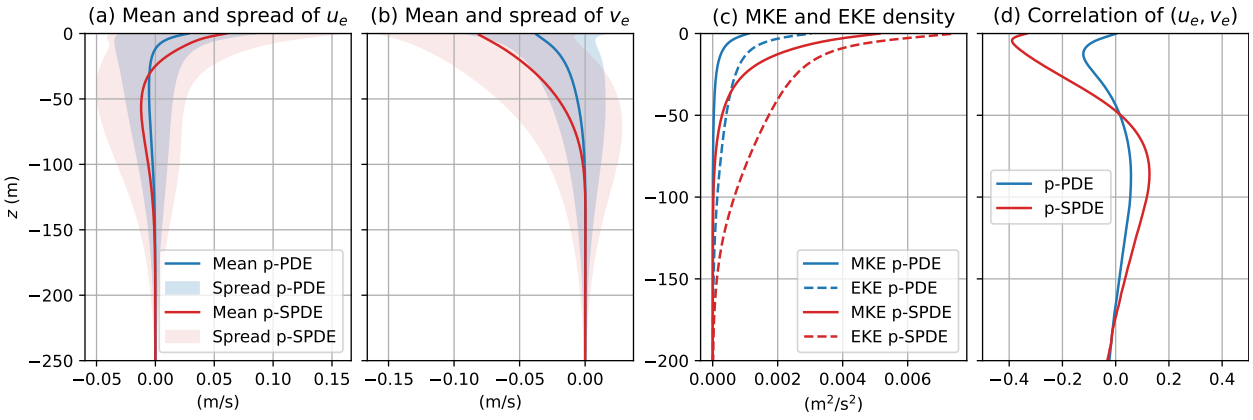

FIG. 3. Comparison of the ensemble mean (solid lines in (a) and (b)) and spread (shaded areas in (a) and (b)) for the Ekman velocity components, the ensemble mean kinetic energy density (solid lines in (c)) and eddy kinetic energy density (dashed lines in (c)), as well as the Pearson correlation coefficient for the Ekman velocity components (d), using different random models (represented by different colors). Note that these ensemble statistics are averaged over the last 20 days of a 30-day simulation.

Higher-order ensemble statistics of the random models can also be examined. The local skewness and kurtosis of the Ekman velocity components over time and depth are illustrated in Fig. 4. The skewness measures the asymmetry of distribution around its mean, and the (excess) kurtosis measures the "tailedness" of the distributions, i.e., the extremity of large values. It is common practice to include a -3 correction for the kurtosis estimator to provide a simple comparison to the (univariate) normal distribution, which has a zero value in that case. Distributions with positive (resp. negative) kurtosis produce more (resp. fewer) extreme events than the normal distribution. Skewness and kurtosis in the upper 100m-depth are shown in Fig. 4, noting that these

normalized statistics are not well-defined for the deeper regions with poor variance. Compared to the p-PDE, the p-SPDE frequently exhibits more positive skew for the zonal component (Fig. 4 (a,e)), more negative skew and for the meridional component (Fig. 4 (b,f)), and more extremes for both components (Fig. 4 (c,d,g,h)), all predominantly occurring in the upper 50 m.

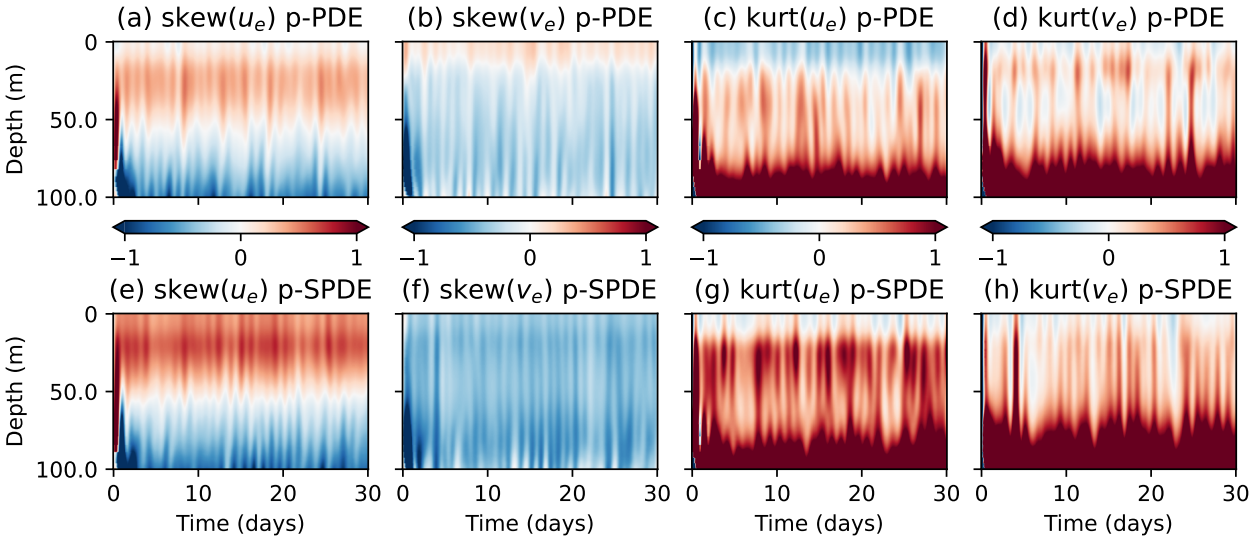

FIG. 4. Comparison of the ensemble skewness and kurtosis for the Ekman velocity components over time and depth using different random models (grouped by rows). A one-day low-pass filtering is applied to these time series of statistics at each point.

Statistical analyses are also conducted on the vertically integrated Ekman transport, Fig. 5. Compared to the p-PDE, the zonal transport component of the p-SPDE exhibits the same zero mean but higher uncertainties over time (Fig. 5 (a)), and almost the same zero skew but with slightly more extremes (Fig. 5 (c)). The meridional transport component of the p-SPDE shows a larger mean in magnitude with higher variance (Fig. 5 (b)), as well as more negative skew and more frequent extremes (Fig. 5 (d)).

The bi-variate PDFs for both instantaneous and time-averaged surface current velocity and Ekman transport are estimated and illustrated Fig. 6. Unsurprisingly, the p-SPDE exhibits higher variances than the p-PDE in both cases. Notably, the p-SPDE demonstrates a much stronger negative correlation for the surface current velocity compared to the p-PDE, which is consistent with the PCC shown in Fig.3 (d). For the proposed random model, the PDF of the surface current appears to be rotated approximately by 45 degrees to the left from the PDFs of the wind and wave

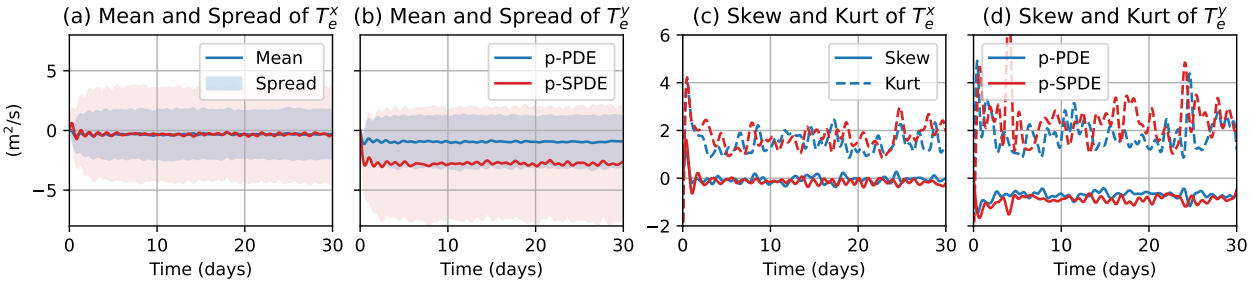

FIG. 5. Time evolution of the ensemble statistics for the Ekman transport components using various random models (distinguished by colors). The solid lines and shaded areas respectively represent the mean and spread in (a) and (b). The solid and dashed lines respectively depict the skewness and kurtosis in (c) and (d). A one-day low-pass filter is applied to these time series of statistics.

stresses (Fig. 2 (b,d)), while the PDF of Ekman transport seems to be rotated approximately by 90 degrees to the left from those surface stresses.

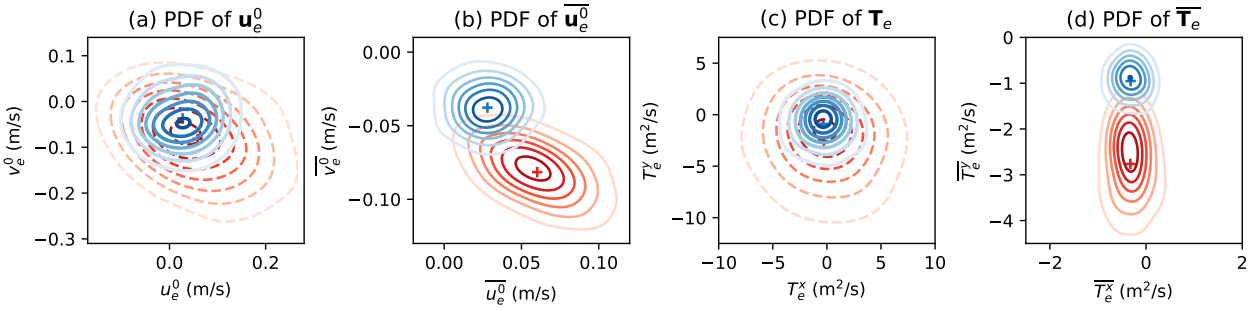

FIG. 6. Comparison of PDFs for (a) instantaneous surface Ekman velocity ($\mathbf{u}_e^0$) after 30 days and (b) its time-average ($\overline{\mathbf{u}_e^0}$) over the last 20 days, as well as for (c) instantaneous Ekman transport ($\mathbf{T}_e$) and (d) its time-average ($\overline{\mathbf{T}_e}$), using different random models (p-PDE in blue and p-SPDE in red). In each panel, the colored signs"+" indicate the mean.

To further highlight the differences between the two schemes, the wind is stopped after 30 days of simulation, by setting $\tau_w = 0$, while maintaining the last day's coefficient a_{zz} as a steady diffusion together with a stationary Stokes drift $\mathbf{u}_s$. The two random models are then run without surface momentum flux for several more days. Results, Fig. 7, demonstrate significant differences in their statistics. For instance, the mean Ekman spiral size of the p-PDE (Fig. 7a) quickly shrinks (the Ekman current profile becomes nearly centered at the origin) whereas the p-SPDE (Fig. 7b) almost preserves its mean spiral structure. Only its current speed decreases over time. Figures 7 (c,

d) show that both the mean and spread of the surface current speed $|\mathbf{u}_e^0|$, as well as the Ekman transport magnitude $|\mathbf{T}_e|$ for the two random models, rapidly decrease, reaching both steady states within one week. However, the residual mean values and uncertainties are significantly higher in the p-SPDE than in the p-PDE. This can be understood from equations (2.16), (2.17) and (2.22b) with $\boldsymbol{\tau}_w = 0$. These results indicate that the p-SPDE transitions from a wind- and wave-driven model to a wave-driven model after the wind stops.

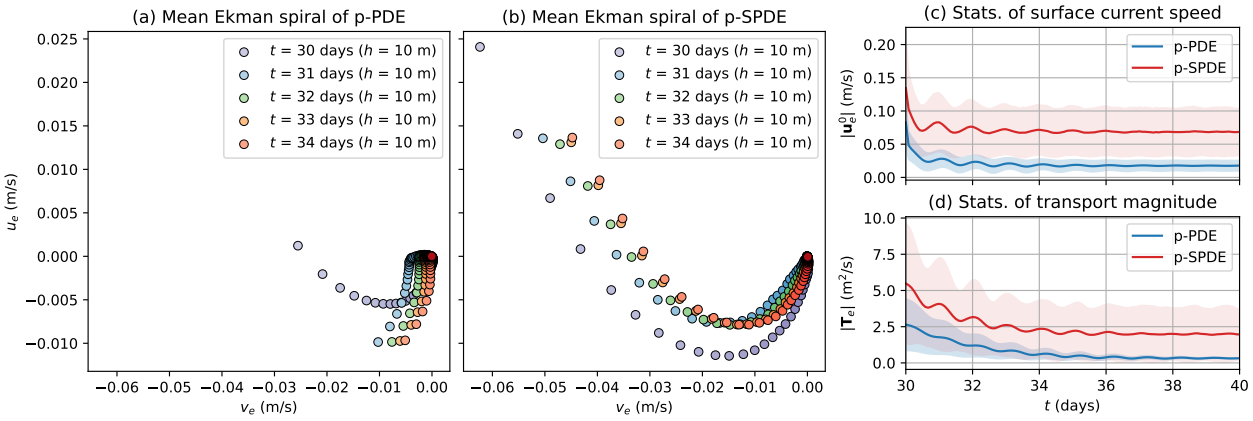

FIG. 7. Evolution comparison after wind stopped for (a, b) mean Ekman spiral, (c) mean and spread of surface current speed, and (d) mean and spread of Ekman transport magnitude, using different random models. The wind is stopped after 30 days of simulation. The mean Ekman spirals at different days in (a, b) are represented by various colors. In each spiral, a darker color indicates a deeper position, with a depth step of 5 meters between adjacent points.

b. Comparison across transient wind levels

Sensitivity analyses to the wind gustiness are performed for the p-SPDE. For this purpose, various ensembles are simulated according to a range of Σ_a values while keeping the other parameters in Table 1 invariant. Illustrated in Fig. 8 (a,b), a higher variable wind reduces the vertical shear of the mean Ekman current, induces deeper circulation, and results in higher uncertainty. Figure 8 (c) demonstrates that increased wind variability leads to larger MKE and EKE throughout the depth, and in particular near the surface. Figure 8 (d) shows weaker negative correlation at the surface but with stronger variations. As described in Section 2e, increased gustiness results in a higher diffusion coefficient a_{zz} (and hence a higher magnitude of the correlation σ_z for the unresolved

motions). It also leads to a larger derived surface wave stress $\boldsymbol{\tau}_s^0$, which amplifies both the wave mixing and stochastic transport effects in the p-SPDE.

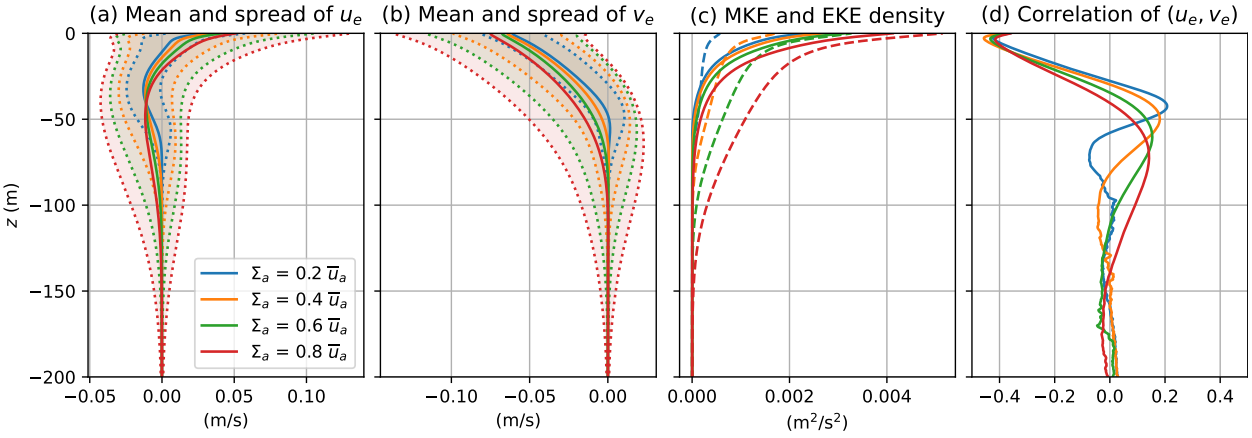

FIG. 8. Comparison of the ensemble mean (solid lines in (a) and (b)) and spread (shaded areas in (a) and (b)) for the Ekman velocity components, the MKE density (solid lines in (c)) and EKE density (dashed lines in (c)), and the correlation coefficient for the Ekman velocity components (d), with respect to different transient wind levels (represented by different colors).

The ensemble skewness and kurtosis of the zonal Ekman velocity component with respect to different Σ_a values are illustrated Fig. 9. More skewed distributions with higher kurtosis are obtained, reflecting an increase in extreme events over time and near the surface. Not shown, similar results were observed for the meridional component.

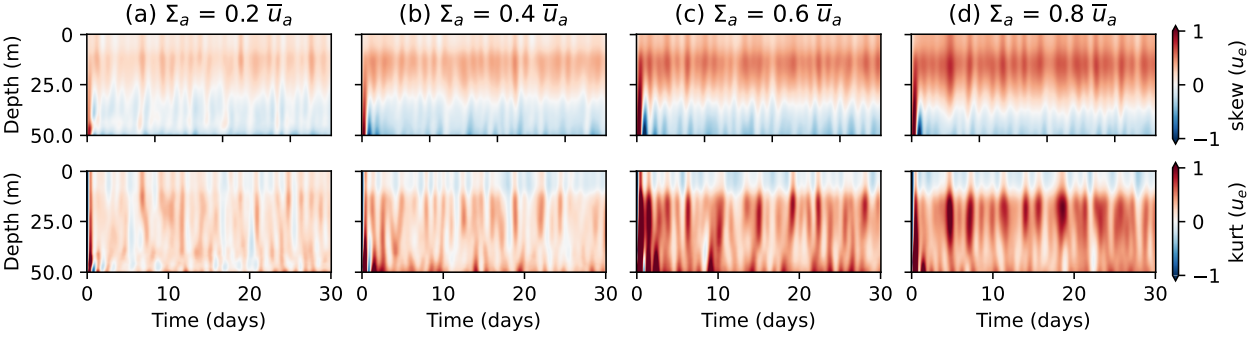

FIG. 9. Comparison of the ensemble kurtosis for the zonal Ekman velocity component over time and depth with respect to different transient wind levels (grouped by columns).

To further quantify the sensitivity to a wider range of Σ_a values, we focus on the time-averaged ensemble statistics of diagnostic variables. Figure 10 (a) shows that both global MKE and EKE

increase with higher transient wind, with EKE rising more rapidly than MKE, especially when the transient wind exceeds half of the mean wind component. Figure 10 (b) demonstrates that both the mean and variance of the estimated boundary layer depth increase with transient wind. Figure 10 (c) illustrates that the Ekman transport magnitude $|\mathbf{T}_e|$ significantly grows with wind. Figure 10 (d) indicates that the mean angle of $\mathbf{T}_e$ is around 100 degrees (relative to the left of the mean wind direction) with a slight increasing trend, while the uncertainty of this angular distribution increases rapidly with wind.

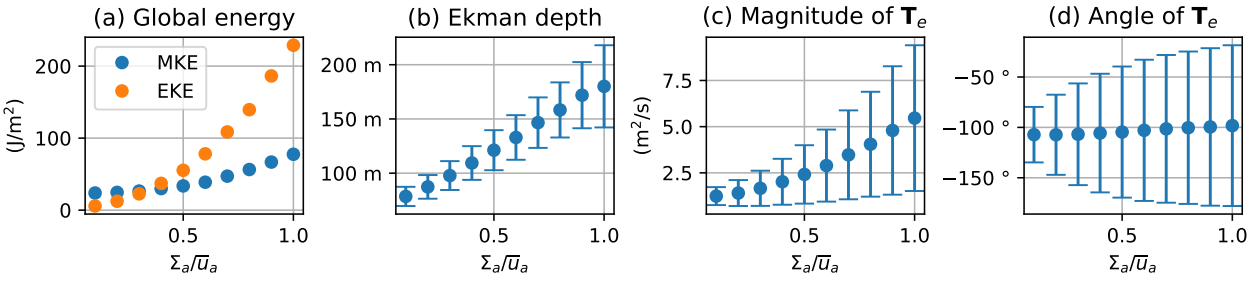

FIG. 10. Comparison of the ensemble statistics for diagnostic variables across various transient wind levels. The MKE and EKE are represented by different colors in (a). The mean and uncertainty are depicted using error bars in (b)-(d). These ensemble statistics are averaged over the last 20 days. It is noteworthy that circular statistics (Fisher 1993) are particularly computed in (d).

c. Comparison across wave parameters

Next, the sensitivity analyses is performed for the p-SPDE to the wavelength λ (or wavenumber k) and the mean angle Θ_s of the Stokes drift, respectively. The same metrics are used in the following analysis.

1) WAVELENGTH

Fig. 11 evidences that a smaller surface gravity wave results in smoother vertical profiles of the mean Ekman current with higher uncertainty (a,b), higher densities of MKE and EKE (c), and stronger correlation (d). These trends are particularly notable near the surface. Furthermore, as shown in Fig. 12 (a,c), both global MKE and EKE, as well as the mean and uncertainty of the transport magnitude, decrease with increasing wavelength. Fig. 12 (b) depicts a slight decreasing tendency for the mean and variance of the estimated Ekman layer depth with increasing wavelength.

Additionally, Fig. 12 (d) illustrates an even smaller decreasing trend for the Ekman transport angles. It is worth noting that a smaller wavelength leads to greater magnitude and vertical shear of the Stokes drift, Eq. (2.27a), thereby amplifying the wave mixing effects in the p-SPDE (2.20).

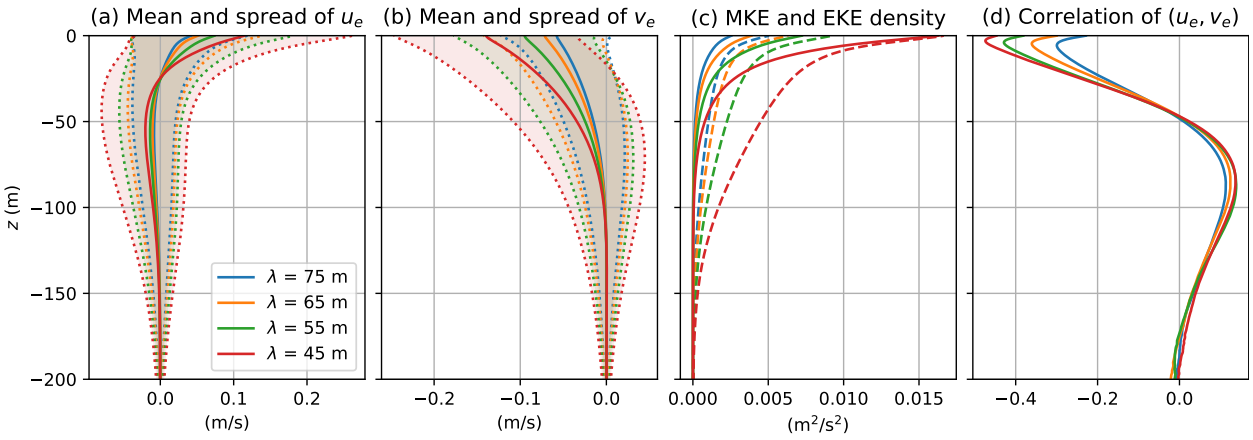

FIG. 11. Comparison of the ensemble mean (solid lines in (a) and (b)) and spread (shaded areas in (a) and (b)) for the Ekman velocity components, the MKE density (solid lines in (c)) and EKE density (dashed lines in (c)), and the correlation coefficient for the Ekman velocity components (d), with respect to different wavelengths.

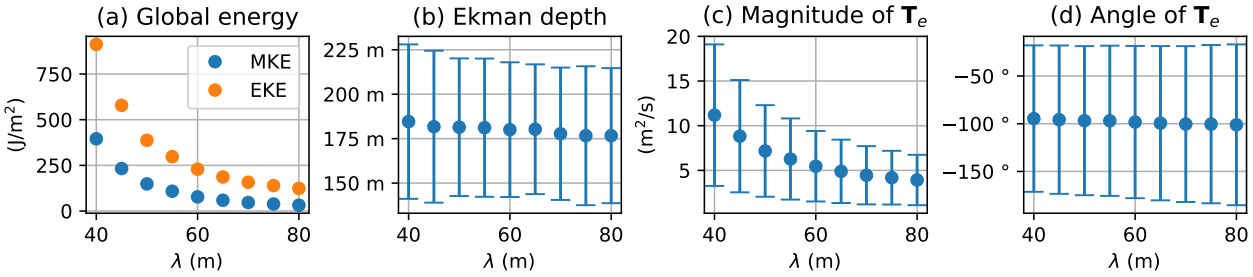

FIG. 12. Comparison of the ensemble statistics for diagnostic variables across various wavelengths.

2) MEAN ANGLE

Fig.13 evidences that waves with a higher rotation from the left of the zonal wind increase both the mean and variance of the zonal Ekman velocity (a) while decreasing those of the meridional component (b) in the upper 100 meters. Additionally, they induce weaker correlation in the upper 25 meters and stronger correlation in the subsequent 50 meters (c). In this scenario, the zonal component exhibits lower positive skew, whereas the meridional component shows higher negative

skew near the surface, Fig.14. This indicates a redistribution of the ensemble statistics between the two components.

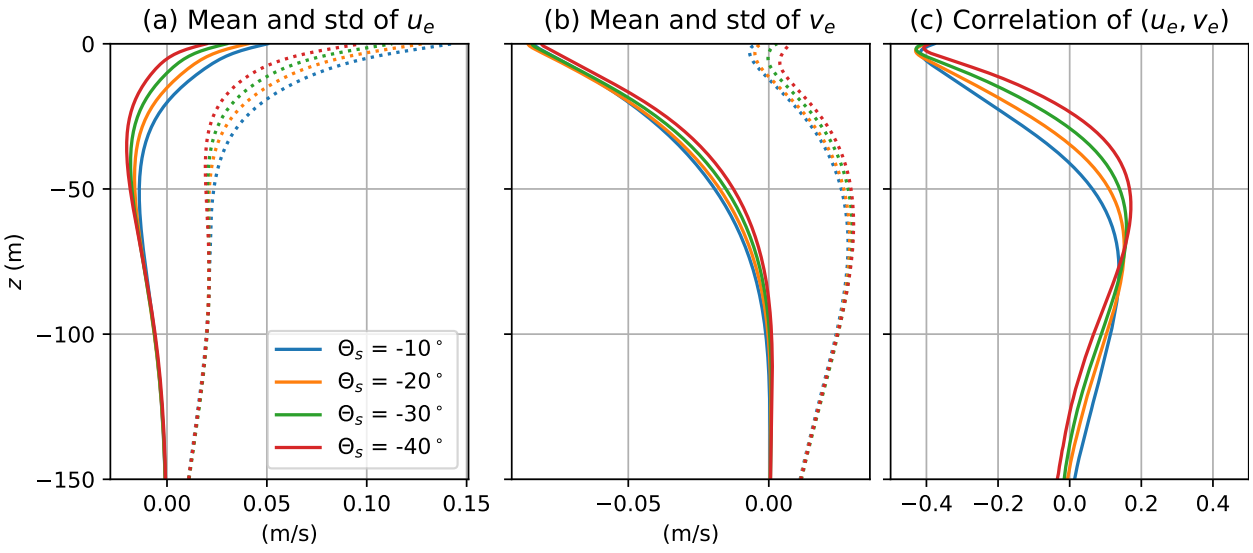

Fig. 13. Comparison of the ensemble mean and std (respectively represented by solid lines in (a) and (b)) and the correlation coefficients (c) for the Ekman velocity components, with respect to different mean angles.

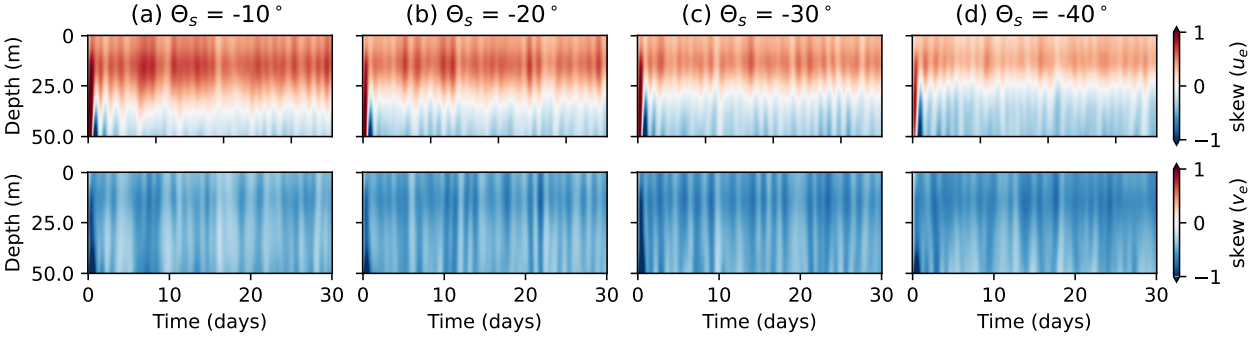

Fig. 14. Comparison of the ensemble skewness for the Ekman velocity components over time and depth with respect to different mean angles.

Global metrics, Fig.15 (a,c), further demonstrate that both MKE and EKE, as well as the mean and uncertainty of the transport magnitude, reach a maximum when the mean wave direction is aligned with the mean wind direction, decreasing symmetrically with higher rotations to either side. It is noteworthy that in the aligned case, the derived wave stress simply enhances the wind stress. Unsurprisingly, the response of the Ekman transport angle follows the variation of the mean

wave directions, as shown in Fig.15 (d). The difference between these output and input angles remains almost invariant.

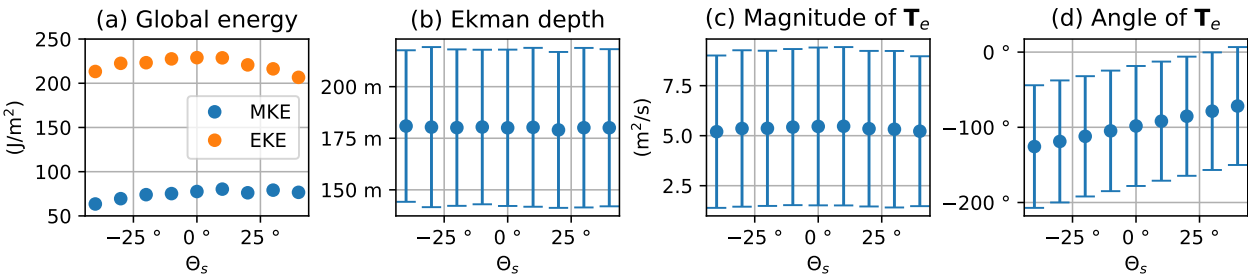

FIG. 15. Comparison of the ensemble statistics for diagnostic variables across various mean angles.

4. Conclusions

In this study, a novel stochastic formulation is developed to describe the upper ocean Ekman boundary layer. This formulation couples the contributions of random fluctuations with the boundary layer dynamics through an uncertainty representation of unresolved motions, fully consistent with established physical parameterizations.

Through numerical investigations, the statistical responses of the proposed time-dependent stochastic Ekman-Stokes model are analyzed. Comparisons are performed with a benchmark model solely driven by the Coriolis-Stokes force. Incorporating wave mixing and stochastic transport compound effects, the stochastic model exhibits smoother mean Ekman velocity profiles with increased uncertainty, along with higher mean kinetic energy (MKE) and eddy kinetic energy (EKE). Additionally, numerical results display stronger correlations between zonal and meridional components, with higher-order statistics indicating more skewed distributions and extreme value occurrences, particularly near the surface.

Sensitivity analyses revealed that increased wind variability reduces vertical shear, deepens circulation, and increases uncertainty and higher-order moments. Similarly, smaller surface waves would lead to higher MKE, EKE, and stronger correlations. Ensemble energy and Ekman transport magnitude peak when mean waves and wind were aligned, decrease with wind-wave misalignment, redistributing current velocity statistics. In terms of sensitivity, the primary source of uncertainty is associated with the wind, followed by the waves, with their direction being the final source of

uncertainty. These findings underscore the enhanced capability of the proposed model to possibly capture and interpret the complex interactions and dynamics of Ekman currents.

Looking ahead, future research avenues include extending the stochastic Ekman-Stokes model to incorporate stratification effects (Price and Sundermeyer 1999; McWilliams et al. 2009; Gula et al. 2014; McWilliams et al. 2015) and exploring the distinct impacts of wave mixing and stochastic transport on thermal front evolution (Crowe and Taylor 2018, 2019). It is important to point out that the retro-action of the waves, possibly modulated by upper ocean random currents, on the wind stress, particularly on the atmospheric wave-induced turbulent components (Ayet and Chapron 2022), has not been taken into account in this study. Along the proposed stochastic framework, developing more accurate noise term to better represent fully coupled ocean/atmosphere Ekman models (Lewis and Belcher 2004) would be particularly interesting.

Additionally, further investigation of the nonlinear stochastic Craik-Leibovich equations through numerical studies, particularly employing large-eddy simulations (LES) to include ocean Langmuir circulation (McWilliams et al. 1997; Harcourt and D'Asaro 2008; McWilliams et al. 2012; Sullivan and McWilliams 2019), offers promising directions for advancing our understanding of turbulent ocean processes and enhancing predictive capabilities.

Acknowledgments. The authors acknowledge the support of the ERC EU project 856408-STUOD.

Data availability statement. The code to reproduce the simulation data, diagnostics, and figures can be accessed at `https://github.com/matlong/SGESM`.

APPENDIX A

Numerical schemes

A pseudo-spectral Chebyshev method (Boyd 2001) is employed for the vertical discretization of the boundary layer models. The so-called *Chebyshev points*, denoted as $\widehat{z}_j = \cos(j\pi/N_z), j = 0,\ldots,N_z$, are depicted in Fig. A1. Geometrically, these points represent the projections on $[-1,1]$ of equispaced points on the upper half of the unit circle. Hence, the projection nodes are denser near the two boundaries than in the mid-regions, which proves advantageous for boundary layer problems and for representing the Stokes drift near the ocean surface. The grid points of the vertical domain depth H are constructed using a linear transformation, $z_j = -H(\widehat{z}_j + 1)/2$. Then, the Chebyshev spectral derivative and integration operators are built on these points to solve a (S)PDE for non-periodic functions with high accuracy.

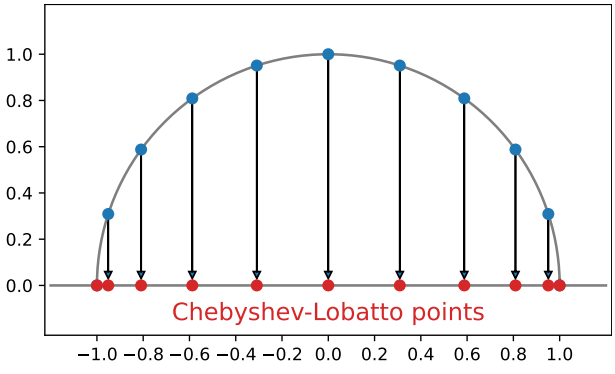

FIG. A1. Geometrical visualization of Chebyshev points (red points) as the projections on $[-1,1]$ of equally spaced points on the upper half of unit circle.

A linear-implicit Euler scheme (Jentzen and Kloeden 2011, chap. 8) is used for the time stepping of the SPDE (2.20), namely

$$\mathbf{u}_j^{n+1} = (I_{j,k} - A_{j,k}\Delta t)^{-1}\left(\mathbf{u}_k^n + F_k^n(\mathbf{u}_s)\Delta t + G_k^n(\mathbf{u}^n,\mathbf{u}_s)\Delta B\right), \tag{A1}$$

Here, $\mathbf{u}_j^n$ denotes the discrete value of the Ekman current velocity $\mathbf{u}_e$ on the node z_j at time t_n, $A = -ifI + Da_{zz}D$ represents the discrete linear operator of the SPDE, where I denotes the identity matrix and D represents the Chebyshev differentiation matrix (Trefethen 2000, chap. 6). The terms F and G correspond to the right-hand side forcing term of Eq. (2.20a).

Additionally, we consider an exact scheme for the wind using the Markovian property of the Ornstein-Uhlenbeck process (2.24), expressed as:

$$\mathbf{u}_a^{n+1} = \overline{\mathbf{u}}_a + (\mathbf{u}_a^n - \overline{\mathbf{u}}_a)e^{-\Delta t/T_a} + \Sigma_a\sqrt{1 - e^{-2\Delta t/T_a}}\boldsymbol{\xi}^n, \tag{A2}$$

Here, $\xi^n = \xi_x^n + i\xi_y^n$ where ξ_x^n and ξ_y^n are independent random variables following a standard normal distribution.

References

Ayet, A., and B. Chapron, 2022: The dynamical coupling of wind-waves and atmospheric turbulence: A review of theoretical and phenomenological models. *Bound.-Lay. Meteorol.*, **183**, 1–33, https://doi.org/10.1007/s10546-021-00666-6.

Bauer, W., P. Chandramouli, B. Chapron, L. Li, and E. Mémin, 2020: Deciphering the role of small-scale inhomogeneity on geophysical flow structuration: a stochastic approach. *J. Phys. Oceanogr.*, **50 (4)**, 983–1003, https://doi.org/10.1175/JPO-D-19-0164.1.

Boyd, J. P., 2001: *Chebyshev and Fourier Spectral Methods*. 2nd ed., Dover Publications, 336 pp.

Brecht, R., L. Li, W. Bauer, and E. Mémin, 2021: Rotating shallow water flow under location uncertainty with a structure-preserving discretization. *J. Adv. Model. Earth Syst.*, **13 (12)**, e2021MS002 492, https://doi.org/10.1029/2021MS002492.

Craik, A., and S. Leibovich, 1976: A rational model for Langmuir circulations. *J. Fluid Mech.*, **73 (3)**, 401–426, https://doi.org/10.1017/S0022112076001420.

Crowe, M. N., and J. R. Taylor, 2018: The evolution of a front in turbulent thermal wind balance. Part 1. theory. *J. Fluid Mech.*, **850**, 179–211, https://doi.org/10.1017/jfm.2018.448.

Crowe, M. N., and J. R. Taylor, 2019: The evolution of a front in turbulent thermal wind balance. Part 2. numerical simulations. *J. Fluid Mech.*, **880**, 326–352, https://doi.org/doi:10.1017/jfm.2019.688.

Da Prato, G., and J. Zabczyk, 2014: *Stochastic equations in infinite dimensions*. 2nd ed., Encyclopedia of Mathematics and its Applications, Cambridge University Press.

Debussche, A., B. Hug, and E. Mémin, 2023: A consistent stochastic large-scale representation of the Navier-Stokes equations. *Journal of Mathematical Fluid Mechanics*, **25 (1)**, 19.

Ekman, V. W., 1905: On the influence of the earth's rotation on ocean-currents. *Ark. Mat. Astr. Fys.*, **2 (11)**, 1–52.

Fisher, N. I., 1993: *Statistical Analysis of Circular Data*. Cambridge University Press.

Fox-Kemper, B., L. Johnson, and F. Qiao, 2022: Ocean near-surface layers. *Ocean Mixing*, Elsevier, 65–94, https://doi.org/10.1016/B978-0-12-821512-8.00011-6.

Gula, J., M. J. Molemaker, and J. C. McWilliams, 2014: Submesoscale cold filaments in the Gulf Stream. *J. Phys. Oceanogr.*, **44 (10)**, 2617–2643, https://doi.org/10.1175/JPO-D-14-0029.1.

Harcourt, R. R., 2013: A second-moment closure model of Langmuir turbulence. *J. Phys. Oceanogr.*, **43 (4)**, 673–697, https://doi.org/10.1175/JPO-D-12-0105.1.

Harcourt, R. R., 2015: An improved second-moment closure model of Langmuir turbulence. *J. Phys. Oceanogr.*, **45 (1)**, 84–103, https://doi.org/10.1175/JPO-D-14-0046.1.

Harcourt, R. R., and E. A. D'Asaro, 2008: Large-eddy simulation of Langmuir turbulence in pure wind seas. *J. Phys. Oceanogr.*, **38 (7)**, 1542–1562, https://doi.org/10.1175/2007JPO3842.1.

Higgins, C., J. Vanneste, and T. S. van den Bremer, 2020: Unsteady Ekman-Stokes dynamics: Implications for surface wave-induced drift of floating marine litter. *Geophys. Res. Lett.*, **47 (18)**, e2020GL089 189, https://doi.org/10.1029/2020GL089189.

Huang, N. E., 1971: Derivation of Stokes drift for a deep-water random gravity wave field. *Deep-Sea Res.*, **18 (2)**, 255–259, https://doi.org/10.1016/0011-7471(71)90115-X.

Huang, N. E., 1979: On surface drift currents in the ocean. *J. Fluid Mech.*, **91 (1)**, 191–208, https://doi.org/10.1017/S0022112079000112.

Jenkins, A. D., 1986: A theory for steady and variable wind-and wave-induced currents. *J. Phys. Oceanogr.*, **16 (8)**, 1370–1377, https://doi.org/10.1175/1520-0485(1986)016⟨1370:ATFSAV⟩2.0.CO;2.

Jenkins, A. D., 1989: The use of a wave prediction model for driving a near- surface current model. *Dtsch. Hydrogr. Z.*, **42**, 134–149, https://doi.org/10.1007/BF02226291.

Jentzen, A., and P. E. Kloeden, 2011: *Taylor Approximations for Stochastic Partial Differential Equations*. Society for Industrial and Applied Mathematics, https://doi.org/10.1137/1.9781611972016.

Large, W. G., J. C. McWilliams, and S. C. Doney, 1994: Oceanic vertical mixing: A review and a model with a nonlocal boundary layer parameterization. *Rev. Geophys.*, **32 (4)**, 63–403, https://doi.org/10.1029/94RG01872.

Le Gall, J., 2016: *Brownian Motion, Martingales, and Stochastic Calculus*. Graduate Texts in Mathematics, Springer International Publishing.

Leibovich, S., 1980: On wave-current interaction theories of Langmuir circulations. *J. Fluid Mech.*, **99 (4)**, 715–724, https://doi.org/10.1017/S0022112080000857.

Lewis, D. M., and S. E. Belcher, 2004: Time-dependent, coupled, Ekman boundary layer solutions incorporating Stokes drift. *Dyn. Atmos. Oceans*, **37 (4)**, 313–351, https://doi.org/10.1016/j.dynatmoce.2003.11.001.

Li, L., B. Deremble, N. Lahaye, and E. Mémin, 2023a: Stochastic data-driven parameterization of unresolved eddy effects in a baroclinic quasi-geostrophic model. *J. Adv. Model. Earth Syst.*, **15 (2)**, e2022MS003 297, https://doi.org/10.1029/2022MS003297.

Li, L., E. Mémin, and G. Tissot, 2023b: Stochastic parameterization with dynamic mode decomposition. *Stochastic Transport in Upper Ocean Dynamics*, Springer, Mathematics of Planet Earth, Vol. 10, 179–193, https://doi.org/10.1007/978-3-031-18988-3_11.

McWilliams, J. C., J. Gula, M. J. Molemaker, L. Renault, and A. F. Shchepetkin, 2015: Filament frontogenesis by boundary layer turbulence. *J. Phys. Oceanogr.*, **45 (8)**, 1988–2005, https://doi.org/10.1175/JPO-D-14-0211.1.

McWilliams, J. C., and E. Huckle, 2006: Ekman layer rectification. *J. Phys. Oceanogr.*, **36 (8)**, 1646–1659, https://doi.org/10.1175/JPO2912.1.

McWilliams, J. C., E. Huckle, J.-H. Liang, and P. P. Sullivan, 2012: The wavy Ekman layer: Langmuir circulations, breaking waves, and Reynolds stress. *J. Phys. Oceanogr.*, **42 (11)**, 1793–1816, https://doi.org/10.1175/JPO-D-12-07.1.

McWilliams, J. C., E. Huckle, and A. F. Shchepetkin, 2009: Buoyancy effects in a stratified Ekman layer. *J. Phys. Oceanogr.*, **39 (10)**, 2581–2599, https://doi.org/10.1175/2009JPO4130.1.

McWilliams, J. C., P. P. Sullivan, and C.-H. Moeng, 1997: Langmuir turbulence in the ocean. *J. Fluid Mech.*, **334**, 1–30, https://doi.org/10.1017/S0022112096004375.

Mellor, G. L., and T. Yamada, 1982: Development of a turbulence closure model for geophysical fluid problems. *Rev. Geophys.*, **20 (4)**, 851–875, https://doi.org/10.1029/RG020i004p00851.

Mémin, E., 2014: Fluid flow dynamics under location uncertainty. *Geophys. Astrophys. Fluid Dyn.*, **108 (2)**, 119–146, https://doi.org/10.1080/03091929.2013.836190.

Mikulevicius, R., and B. Rozovskii, 1998: Linear parabolic stochastic PDE and Wiener Chaos. *SIAM Journal on Mathematical Analysis*, **29 (2)**, 452–480, https://doi.org/doi:10.1137/S0036141096299065.

Mikulevicius, R., and B. Rozovskii, 2004: Stochastic Navier–Stokes equations for turbulent flows. *SIAM Journal on Mathematical Analysis*, **35 (5)**, 1250–1310.

Pedlosky, J., 1990: *Geophysical Fluid Dynamics*. 2nd ed., Springer-Verlag, New York, NY, USA, 710 pp.

Phillips, O. M., 1977: *The Dynamics of the Upper Ocean*. Cambridge University Press, 336 pp.

Price, J. F., and M. A. Sundermeyer, 1999: Stratified Ekman layers. *J. Geophys. Res.*, **104 (C9)**, 20 467–20 494, https://doi.org/10.1029/1999JC900164.

Resseguier, V., L. Li, G. Jouan, P. Dérian, E. Mémin, and B. Chapron, 2021: New trends in ensemble forecast strategy: Uncertainty quantification for coarse-grid computational fluid dynamics. *Arch. Computat. Methods Eng.*, **28 (1)**, 215–261, https://doi.org/10.1007/s11831-020-09437-x.

Resseguier, V., E. Mémin, and B. Chapron, 2017: Geophysical flows under location uncertainty, Part I, II & III . *Geophys. & Astro. Fluid Dyn.*, **111 (3)**, 149–227.

Sullivan, P. P., and J. C. McWilliams, 2019: Langmuir turbulence and filament frontogenesis in the oceanic surface boundary layer. *J. Phys. Oceanogr.*, **879**, 512–553, https://doi.org/10.1017/jfm.2019.655.

Trefethen, L. N., 2000: *Spectral Methods in MATLAB*. Society for Industrial and Applied Mathematics, https://doi.org/10.1137/1.9780898719598.

Tucciarone, F. L., E. Mémin, and L. Li, 2024: Data driven stochastic primitive equations with dynamic modes decomposition. *Stochastic Transport in Upper Ocean Dynamics II*, Springer, Mathematics of Planet Earth, Vol. 11, 321–336, https://doi.org/10.1007/978-3-031-40094-0_15.

Vallis, G. K., 2017: *Atmospheric and oceanic fluid dynamics: fundamentals and large-scale circulation*. 2nd ed., Cambridge University Press.

Wenegrat, J. O., and M. J. McPhaden, 2016a: A simple analytical model of the diurnal Ekman layer. *J. Phys. Oceanogr.*, **46 (9)**, 2877–2894, https://doi.org/10.1175/JPO-D-16-0031.1.

Wenegrat, J. O., and M. J. McPhaden, 2016b: Wind, waves, and fronts: Frictional effects in a generalized Ekman model. *J. Phys. Oceanogr.*, **46 (2)**, 371–394, https://doi.org/10.1175/JPO-D-15-0162.1.

Xu, Z., and A. J. Bowen, 1994: Wave- and wind-driven flow in water of finite depth. *J. Phys. Oceanogr.*, **24 (9)**, 1850–1866, https://doi.org/10.1175/1520-0485(1994)024⟨1850:WAWDFI⟩2.0.CO;2.